AFFDL-TR-77-116

AD A054462

AN EXACT VELOCITY POTENTIAL SOLUTION OF STEADY, COMPRESSIBLE FLOW OVER ARBITRARY TWO-DIMENSIONAL AND AXISYMMETRIC BODIES IN SIMPLY CONNECTED FIELDS

Aerodynamics and Airframe Branch
Aeromechanics Division

August 1977

TECHNICAL REPORT AFFDL-TR-77-116

Final Report for Period March 1975 to August 1977

Approved for public release; distribution unlimited.

AD NO.
DDC FILE COPY

D D C
RECEIVED
MAY 31 1978
D

AIR FORCE FLIGHT DYNAMICS LABORATORY
AIR FORCE WRIGHT AERONAUTICAL LABORATORIES
AIR FORCE SYSTEMS COMMAND
WRIGHT-PATTERSON AIR FORCE BASE, OHIO 45433

FOR THE COMMANDER

GUION BLUFORD, MAJOR, USAF
Chief, Aerodynamics and Airframe Branch
Aeromechanics Division

AIR FORCE/56780/31 March 1978 — 100

REPORT DOCUMENTATION PAGE		READ INSTRUCTIONS BEFORE COMPLETING FORM
1. REPORT NUMBER AFFDL-TR-77-116	2. GOVT ACCESSION NO.	3. RECIPIENT'S CATALOG NUMBER
4. TITLE (and Subtitle) AN EXACT VELOCITY POTENTIAL SOLUTION OF STEADY, COMPRESSIBLE FLOW OVER ARBITRARY TWO-DIMENSIONAL AND AXISYMMETRIC BODIES IN SIMPLY CONNECTED FIELDS.		5. TYPE OF REPORT & PERIOD COVERED Final Report. 1 Mar 1975 - 1 Aug 1977
		6. PERFORMING ORG. REPORT NUMBER
7. AUTHOR(s) Thomas J. Plant, 1 Lt, USAF		8. CONTRACT OR GRANT NUMBER(s)
9. PERFORMING ORGANIZATION NAME AND ADDRESS Aerodynamics and Airframe Branch (FXM) Air Force Flight Dynamics Laboratory Wright-Patterson Air Force Base, Ohio 45433		10. PROGRAM ELEMENT, PROJECT, TASK AREA & WORK UNIT NUMBERS Project 1476 Task 147602 Job Order No. 14760221
11. CONTROLLING OFFICE NAME AND ADDRESS		12. REPORT DATE Aug 77
		13. NUMBER OF PAGES
14. MONITORING AGENCY NAME & ADDRESS(if different from Controlling Office)		15. SECURITY CLASS. (of this report) Unclassified
		15a. DECLASSIFICATION/DOWNGRADING SCHEDULE

16. DISTRIBUTION STATEMENT (of this Report)

Approved for public release; distribution unlimited

17. DISTRIBUTION STATEMENT (of the abstract entered in Block 20, if different from Report)

62201F

18. SUPPLEMENTARY NOTES

19. KEY WORDS (Continue on reverse side if necessary and identify by block number)

Potential flow	Curvilinear coordinates
Numerical fluid mechanics	Nozzle afterbody flows
Transonic flow	

20. ABSTRACT (Continue on reverse side if necessary and identify by block number)

This report discusses the use of the automatic numerical generation of curvilinear body fitted coordinates to solve the exact velocity potential equation for steady, compressible flow over two-dimensional and axisymmetric bodies in simply connected fields. A system of partial differential equations consisting of a Poisson equation for each coordinate direction is used to numerically generate the coordinates. A new, fast method of evaluating non-homogeneous terms for application to the Poisson generation system helps to make the

DD FORM 1473 1 JAN 73   EDITION OF 1 NOV 65 IS OBSOLETE   UNCLASSIFIED

SECURITY CLASSIFICATION OF THIS PAGE (When Data Entered)

coordinates more orthogonal. The use of these curvilinear coordinates allows the exact velocity potential equations to be easily applied to diverse body shapes and boundaries.

FOREWORD

This report was prepared by 1/Lt Thomas J. Plant of the Internal
Aerodynamics Group, Aerodynamics and Airframe Branch, Aeromechanics
Division, of the Air Force Flight Dynamics Laboratory, Wright-Patterson
Air Force Base, Ohio. This research was conducted under Work Unit
Number 14760221, "Design and Analysis of Advanced Strategic and
Tactical Military Aircraft Exhaust Nozzle Systems." This research
was conducted from 1 March 1975 to 1 August 1977.

ACCESSION for		
NTIS	White Section	X
DDC	Buff Section	☐
UNANNOUNCED		☐
JUSTIFICATION		
BY		
DISTRIBUTION/AVAILABILITY CODES		
Dist.	AVAIL. and/or SPECIAL	
A		

AFFDL-TR-77-116

TABLE OF CONTENTS

LIST OF ILLUSTRATIONS

LIST OF ILLUSTRATIONS (CONTINUED)

LIST OF ILLUSTRATIONS (CONTINUED)

LIST OF TABLES

LIST OF SYMBOLS

a	Speed of sound
A,B,C,D	Coefficients in transformed velocity potential equation
ABC	Numerical acceleration parameter for boundary condition points
AER	Numerical acceleration parameter for elliptical region points
AHR	Numerical acceleration parameter for hyperbolic region points
A_k, A_k'	Line attraction coefficients used in definition of P and Q
A_1, A_2	Coefficients in transformed velocity potential
B_i, B_i'	Point attraction coefficients used in definition of P and Q
B_1, B_2	Coefficients in transformed velocity potential equation
C_D, C_{D_p}	Integrated pressure drag coefficient
C_k, C_k'	Damping factor coefficients for line attraction portion in definition of P and Q
$\mathcal{L}$	Centerline
C_p	Pressure coefficient
C_p^*	Pressure coefficient where Mach number equals unity
C_1, C_2	Coefficients in transformed velocity potential equation
d( )	Differential increment of ( )
D	Pressure drag Physical domain of dependence
D^*	Transformed (computational) domain of dependence

LIST OF SYMBOLS (CONT.)

D_ℓ, D_ℓ'	Damping coefficient for point attraction portion in definition of P and Q
f	Arbitrary function
f_1, f_2	Functions describing distributions of x,y along Γ_1^*
g_1, g_2	Functions describing distributions of x,y along Γ_2^*
h	Step size in pressure drag integration formula
h_1, h_2	Functions describing distributions of x,y along Γ_3^*
$\hat{i}$	Unit vector in the x-direction
$\hat{j}$	Unit vector in the y-direction
J	Jacobian of coordinate transformation, $J = x_\xi y_\eta - x_\eta y_\xi$
k	Counter
k_1, k_2	Functions describing distributions of x,y along Γ_4^*
k_1, k_2, k_3 k_4, k_5	Coefficients of transformed velocity potential equation
ℓ	Counter
L/D	Body length to maximum body diameter ratio
m, m'	Number at attraction points in definition of P and Q
M	Mach number
n, n'	Number of attraction lines in definition of P and Q
$\hat{n}$	Unit vector normal to the surface
NAB	Nozzle afterbody
NIC	Number of iterations required for convergence
NPR	Nozzle pressure ratio

LIST OF SYMBOLS (CONT.)

P	Pressure
P,Q	Non-homogenous terms of the Poisson equations governing the coordinate system generation
Q	Local total velocity, $Q=(u^2+v^2)^{\frac{1}{2}}$
R	Radial distance from the centerline of axisymmetric bodies
R_e	Reynolds number per foot
R_{e_ℓ}	Reynolds number based on body length
R_ℓ	Coefficient used in definition of P and Q
s	Arc length
S	Surface area
S_{ref}	Reference area for axisymmetric body pressure drag integration - normally maximum cross-sectional area
SOR	Successive-Over-Relaxation iteration
u	Velocity in the x-direction
u^*	Velocity used to implement a stagnation point
v	Velocity in the y-direction
$\underline{v}$	Velocity vector
x,y	Cartesian coordinates
X/L	x-direction non-dimensional body location
α	Control to specify axisymmetric or two-dimensional flow
α,β,γ	Coefficients of coordinate transformation equation
γ_a	Ratio of specific heats of the fluid
$\Gamma_1^*,\Gamma_2^*,\Gamma_3^*,\Gamma_4^*$	Boundaries of the transformed (computational) plane
$\Delta(\ )$	Increment of ( )
ξ,η	Transformed (computational) coordinates
ξ_k,η_k	Attraction lines in definition of P and Q

LIST OF SYMBOLS (CONCLUDED)

ξ_ℓ, η_ℓ	Attraction points in definition of P and Q
ξ_1, η_1	Function describing distribution of ξ, η along Γ_1
ξ_2, η_2	Function describing distribution of ξ, η along Γ_2
ξ_3, η_3	Function describing distribution of ξ, η along Γ_3
ξ_4, η_4	Function describing distribution of ξ, η along Γ_4
ρ	Density
ϕ	Exact velocity potential

SUBSCRIPTS

MAX	Maximum value
x, y, ξ, η	First partial differentiation
$xx, yy, \xi\xi, \eta\eta$	Second partial differentiation
$\xi\eta$	Cross partial differentiation
∞	Free-stream, reference, or ambient condition

SUPERSCRIPTS

(η)	The indicated operator is with respect to an η-surface

SECTION I

INTRODUCTION

During the last decade, many successful computational methods of solution of two-dimensional and axisymmetric transonic flows have appeared. Most early methods (References 6 and 7) depended on simple geometry and the small perturbation potential equation. Jameson (Reference 21) was one of the first to realize the utility of non-Cartesian coordinate systems for the solution of non-simple geometry with the exact velocity potential equation. The present work seeks to extend this idea to include the numerical body-fitted coordinate system generation method developed by Thompson (References 1 and 4). Later work by Thames and Thompson along lines similar to the present work is presented in Reference 22.

In the current work, a quick, simple method of generating simply connected coordinate systems is developed for thin and slender bodies, while Thompson's original grid generation method is reserved for more complex bodies. The mixed differencing scheme of Murman and Krupp (Reference 7) is applied to the transformed exact velocity potential equation. The method is verified by applying it to several bodies of interest.

SECTION II

NUMERICAL GENERATION OF CONTROL VOLUME BOUNDARY -

FITTED CURVILINEAR COORDINATE SYSTEMS

For the numerical solution of fluid flow problems, it would be convenient to have a curvilinear coordinate system whose outer boundaries are coincident with the desired solution control volume. Thompson, Thames, and Mastin (Reference 1) have developed such a numerical method. Thames (Reference 2) provides perhaps the most complete and comprehensive explanation of the method. The first part of this discussion is based on the work of Thames. It provides a basic explanation of the method and the changes made to apply it efficiently to the solution of the full velocity potential equation for compressible two-dimensional and axisymmetric flows in a simply connected region. A brief explanation of the numerical analysis used to complete the transformation is presented.

1. BASIC TRANSFORMATION

Consider transforming an arbitrary two-dimensional, simply connected region, D, such as that shown in Figure 1 onto a rectangular region, D*, as shown in Figure 2. We require that Γ_1 map onto Γ_1^*, Γ_2 onto Γ_2^*, Γ_3 onto Γ_3^*, and Γ_4 onto Γ_4^*. Region D is referred to as the physical plane and region D* as the transformed plane. For the present purposes, Γ_1 is identified as a body surface. Γ_2 and Γ_4 are considered to be straight lines of symmetry for a possible axisymmetric consideration.[+] Γ_3 is taken as an outer boundary. In the present work, Γ_3 will be used as both an "infinity" semi-circle and a straight wind-tunnel wall. Note that all of the transformed boundaries are constant coordinate lines (η-lines) in the transformed plane.

[+] Note that, in this discussion, no generality is lost by this imposed condition, since Γ_1 and Γ_2 are treated as being arbitrarily shaped.
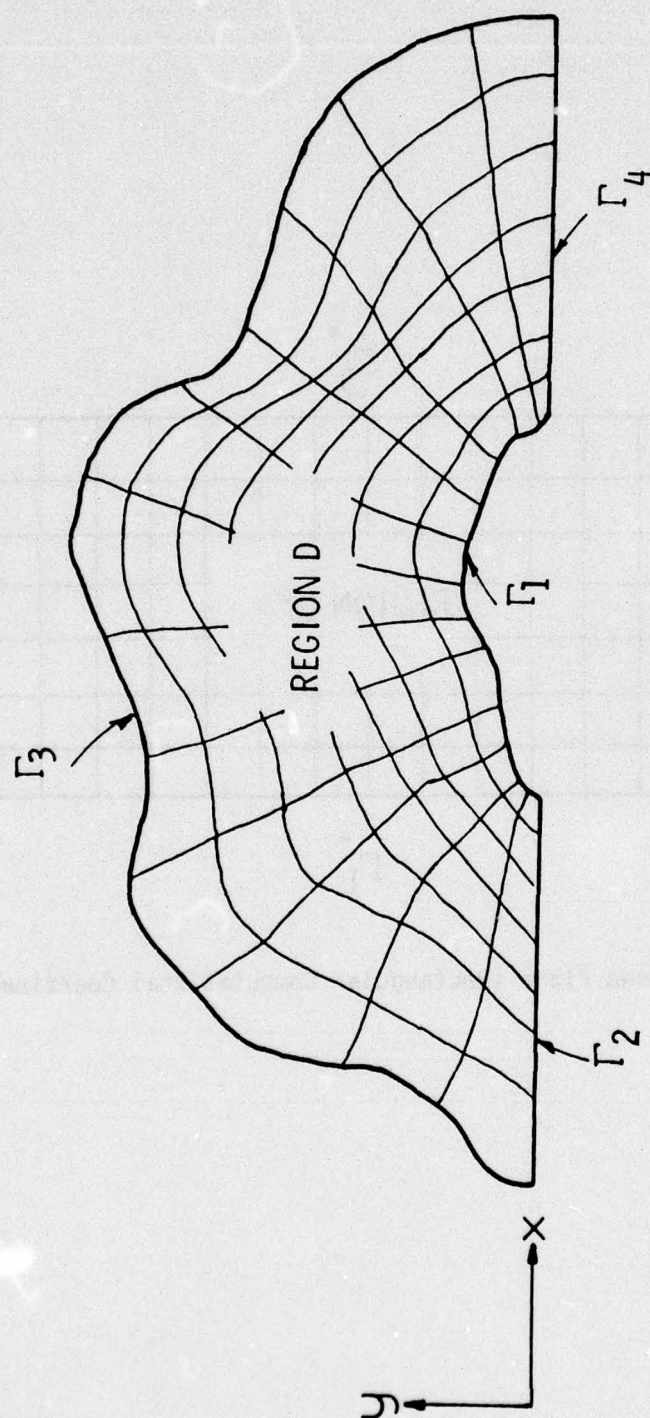
Figure 1. Physical Plane (Natural Body-Fitted Coordinates)
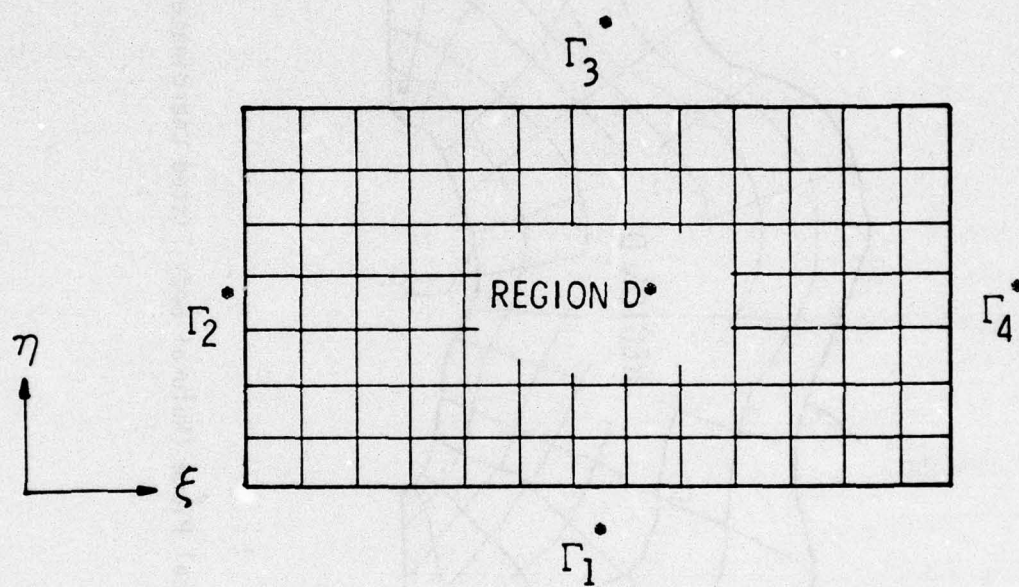
Figure 2. Transformed Plane (Rectangular Computational Coordinates)

For mathematical reasons discussed by Thames (Reference 2), Laplace equations are taken as the generating elliptic system

$$\xi_{xx} + \xi_{yy} = 0 \tag{1}$$

$$\eta_{xx} + \eta_{yy} = 0 \tag{2}$$

with the Dirichlet boundary conditions

$$\begin{bmatrix} \xi \\ \eta \end{bmatrix} = \begin{bmatrix} \xi_1(x,y) \\ \eta_1 \end{bmatrix}, \ (x,y) \ \epsilon \ \Gamma_1 \tag{3}$$

$$\begin{bmatrix} \xi \\ \eta \end{bmatrix} = \begin{bmatrix} \xi_2 \\ \eta_2(x,y) \end{bmatrix}, \ (x,y) \ \epsilon \ \Gamma_2 \tag{4}$$

$$\begin{bmatrix} \xi \\ \eta \end{bmatrix} = \begin{bmatrix} \xi_3(x,y) \\ \eta_3 \end{bmatrix}, \ (x,y) \ \epsilon \ \Gamma_3 \tag{5}$$

$$\begin{bmatrix} \xi \\ \eta \end{bmatrix} = \begin{bmatrix} \xi_4 \\ \eta_4(x,y) \end{bmatrix}, \ (x,y) \ \epsilon \ \Gamma_4 \tag{6}$$

where η_1, ξ_2, η_3, and ξ_4 are constant and $\xi_1(x,y)$, $\eta_2(x,y)$, $\xi_3(x,y)$, and $\eta_4(x,y)$ are specified, non-constant functions on Γ_1, Γ_2, Γ_3, and Γ_4, respectively.

For the method to be practical, it is necessary to perform all numerical computations in the uniform rectangular transformed plane. Following Thames (Reference 2), Equations 1 through 6 transform to the system

$$\alpha x_{\xi\xi} - 2\beta x_{\xi\eta} + \gamma x_{\eta\eta} = 0 \tag{7}$$

$$\alpha y_{\xi\xi} - 2\beta y_{\xi\eta} + \gamma y_{\eta\eta} = 0 \tag{8}$$

where

$$\alpha \equiv x_\eta^2 + y_\eta^2 \tag{9}$$

$$\beta \equiv x_\xi x_\eta + y_\xi y_\eta \tag{10}$$

$$\gamma \equiv x_\xi^2 + y_\xi^2 \tag{11}$$

with the transformed boundary conditions

$$\begin{bmatrix} x \\ y \end{bmatrix} = \begin{bmatrix} f_1(\xi,\eta_1) \\ f_2(\xi,\eta_1) \end{bmatrix}, \ [\xi,\eta] \ \epsilon \ \Gamma_1^* \tag{12}$$

5

$$\begin{bmatrix} x \\ y \end{bmatrix} = \begin{bmatrix} g_1(\xi_2, \eta) \\ g_2(\xi_2, \eta) \end{bmatrix}, \ [\xi, \eta] \ \epsilon \ \Gamma_2^* \tag{13}$$

$$\begin{bmatrix} x \\ y \end{bmatrix} = \begin{bmatrix} h_1(\xi, \eta_3) \\ h_2(\xi, \eta_3) \end{bmatrix}, \ [\xi, \eta] \ \epsilon \ \Gamma_3^* \tag{14}$$

$$\begin{bmatrix} x \\ y \end{bmatrix} = \begin{bmatrix} k_1(\xi_4, \eta) \\ k_2(\xi_4, \eta) \end{bmatrix}, \ [\xi, \eta] \ \epsilon \ \Gamma_4^* \tag{15}$$

The functions f_1, f_2, h_1, and h_2 are specified by the known shape of the boundaries Γ_1 and Γ_3 and the specified distribution of ξ thereon. Similarly, g_1, g_2, k_1, and k_2 are specified by the desired shape of the boundaries Γ_2 and Γ_4 and the specified distribution of η on those boundaries.

The set of Equations 7 through 15 is a quasi-linear elliptic system for the physical coordinates, $x(\xi, \eta)$ and $y(\xi, \eta)$, in the transformed plane. With this system, (x,y) are specified for each (ξ, η) point on the four boundaries. Coordinates (ξ, η) are conveniently numbered as 1, 2, 3, 4, . . ., ξ_{MAX} and 1, 2, 3, . . ., η_{MAX}. This simple numbering is the constant step size in the computational transformed plane. With the boundaries specified, Equations 7 and 8 are numerically solved. The resulting natural coordinate system has an η-line coincident with the Γ_1 and Γ_3 boundaries and an ξ-line coincident with the Γ_2 and Γ_4 boundaries.

Since this method does not produce orthogonal coordinates, the fluid flow equations to be solved[+] on the natural coordinates must be transformed by direct implicit partial differentiation. Thames (Reference 2) gives the derivative expressions for time-dependent, two-dimensional systems, and shows that the type (i.e., elliptic, parabolic, hyperbolic) of the fluid equations does not change under the transformation.

[+]Note that this method applies to any set of partial differential equations.

6

The numerical method used to solve Equations 7 and 8 was based on a modification of a computer code by Thompson (Reference 1) to solve only simply connected regions with various options added that will be discussed later.

As discussed by Thames (Reference 2), a reasonable "initial guess" (i.e., iterate #0) is required to guarantee a converged solution for Equations 7 and 8 when using accelerated successive over relaxation (SOR) iteration. Figures 3 and 4 are samples of coordinate system initial guesses for two bodies for which the compressible transonic velocity potential solutions are discussed in Section IV. Figure 3 is a NACA 0012 airfoil with an outer boundary of a circle of radius-ten body lengths, which represents an "infinity" boundary. The Γ_2 and Γ_4 boundaries are held straight for convenience as lines-of-flow symmetry. The interior of the field is a combination of straight lines and ellipses. Figure 4 is a numerical model of a NASA wind-tunnel model in a simulated NASA Langley Research Center 16T wind tunnel used in an AGARD "Improved Nozzle Testing Techniques" study (Reference 12).

2. EXTENSION OF THE BASIC TRANSFORMATION TO PROVIDE FOR CONTRACTION OF THE GRID

The adjustment of grid spacing may be necessary in areas of high flow gradients. Figures 5 and 6 demonstrate that the solution results of the elliptic system of Equations 7 and 8 are good; however, when the flow gradients are large, the grid is not tight enough to ensure that truncation error does not affect the solution. Also, for an axisymmetric problem, close grid spacing near the axis (y=0) is necessary for an accurate solution. More control can be obtained over both ξ and η-line spacing by alteration of the elliptic system of Equations 7 and 8.

Thompson, et al (Reference 1) have shown that a set of equations of the form

$$\nabla^2 \xi = P(x,y) \tag{16}$$
$$\nabla^2 \eta = Q(x,y) \tag{17}$$

can be formulated with the boundary conditions given in Equations 3 thru 6. $P = P(x,y)$ and $Q = Q(x,y)$ are continuously differentiable negative functions on D and its boundary.

7
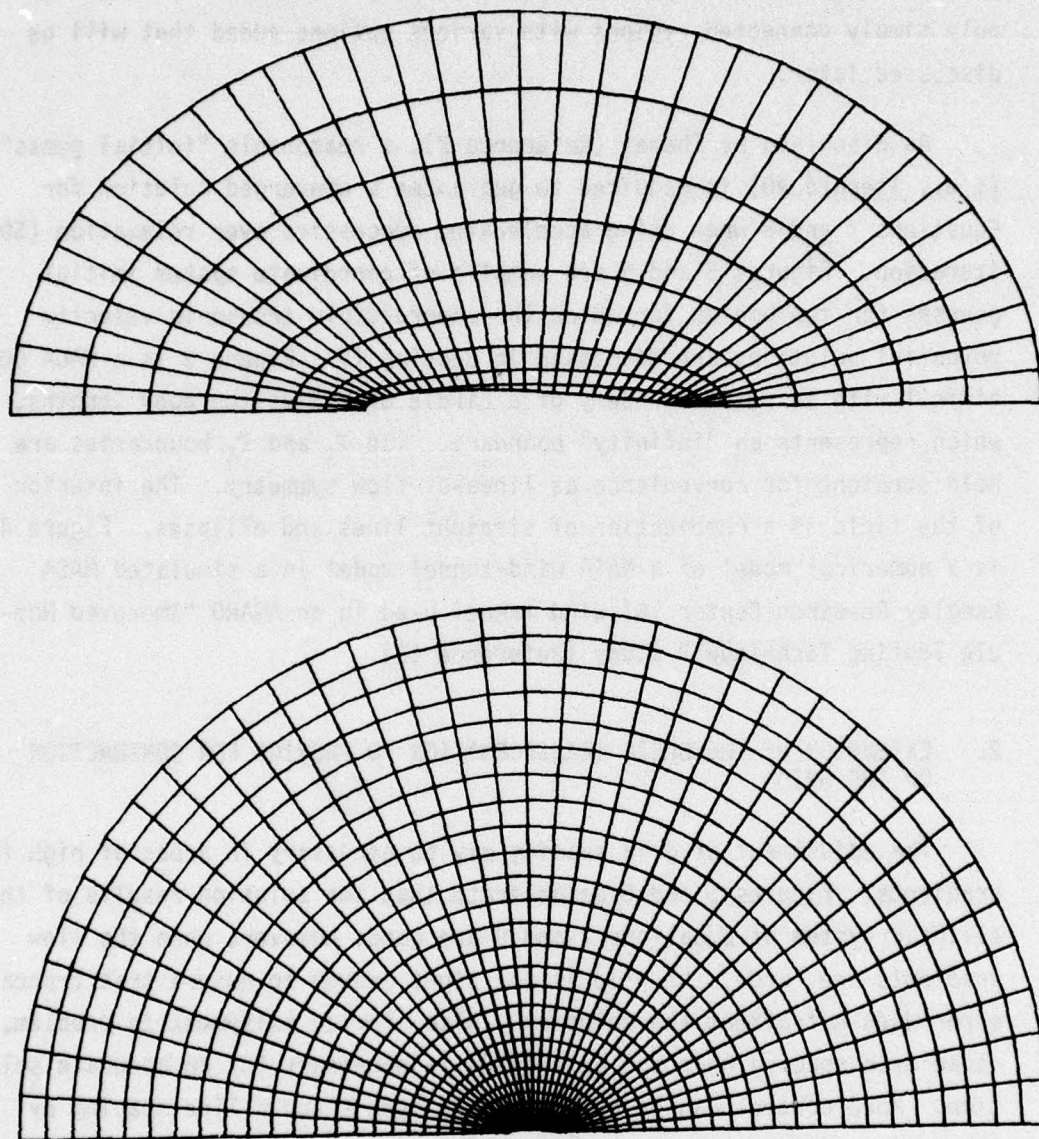
Figure 3.   NACA 0012 Airfoil - Coordinate System Initial Specification
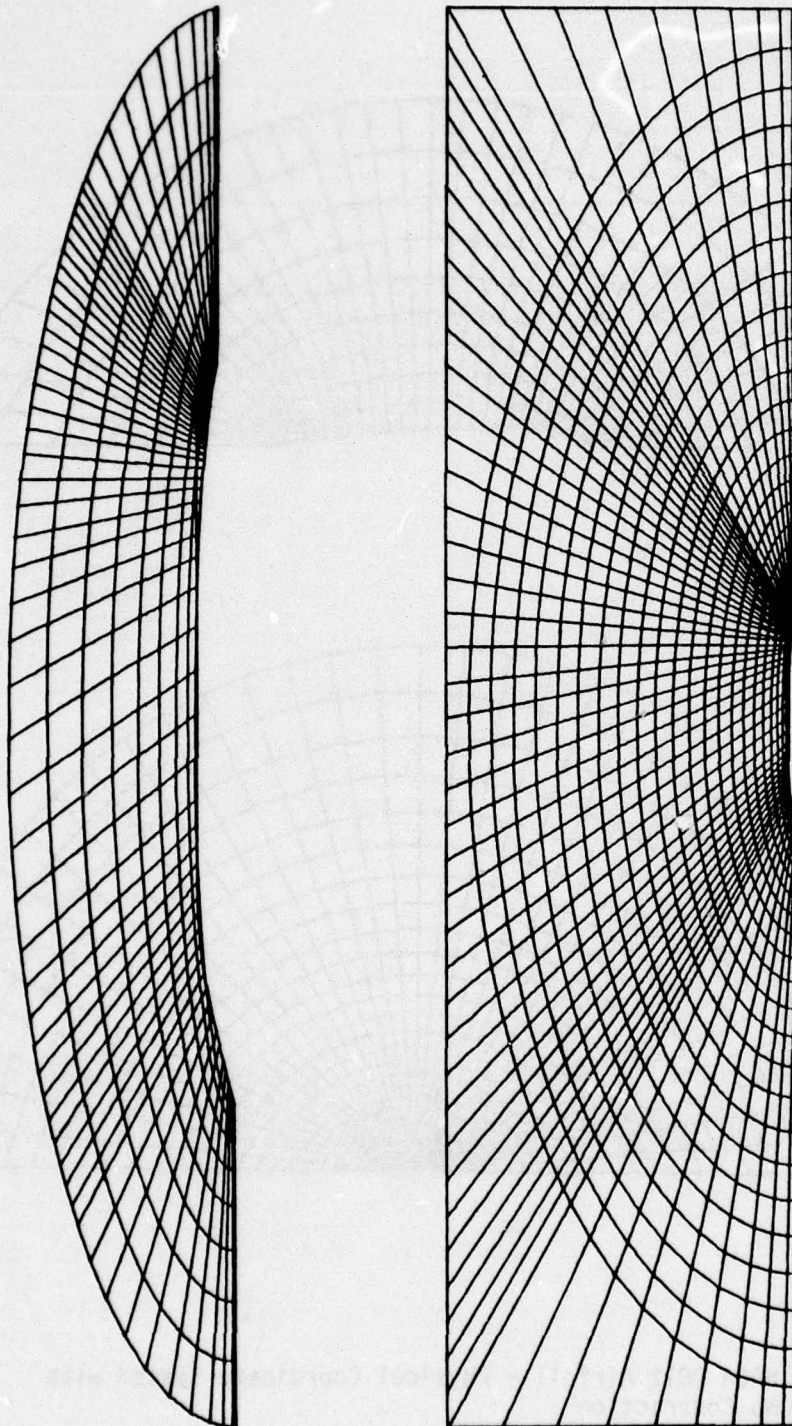
Figure 4. Agard AD HOC Study - NASA Forebody - 15⁰ Boattail - NASA Tunnel Coordinate System Initial Specification
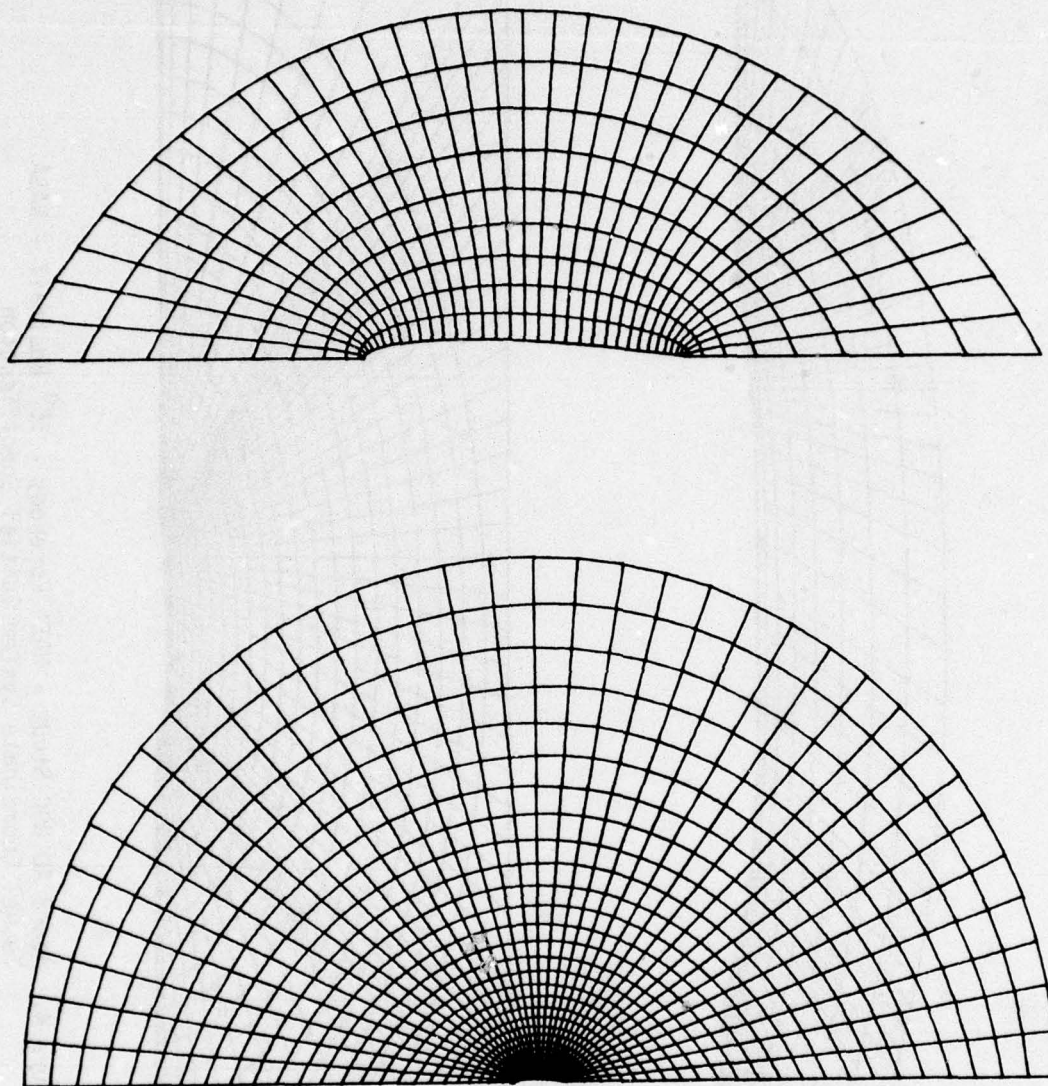
Figure 5. NACA 0012 Airfoil - Physical Coordinate System with No Contraction
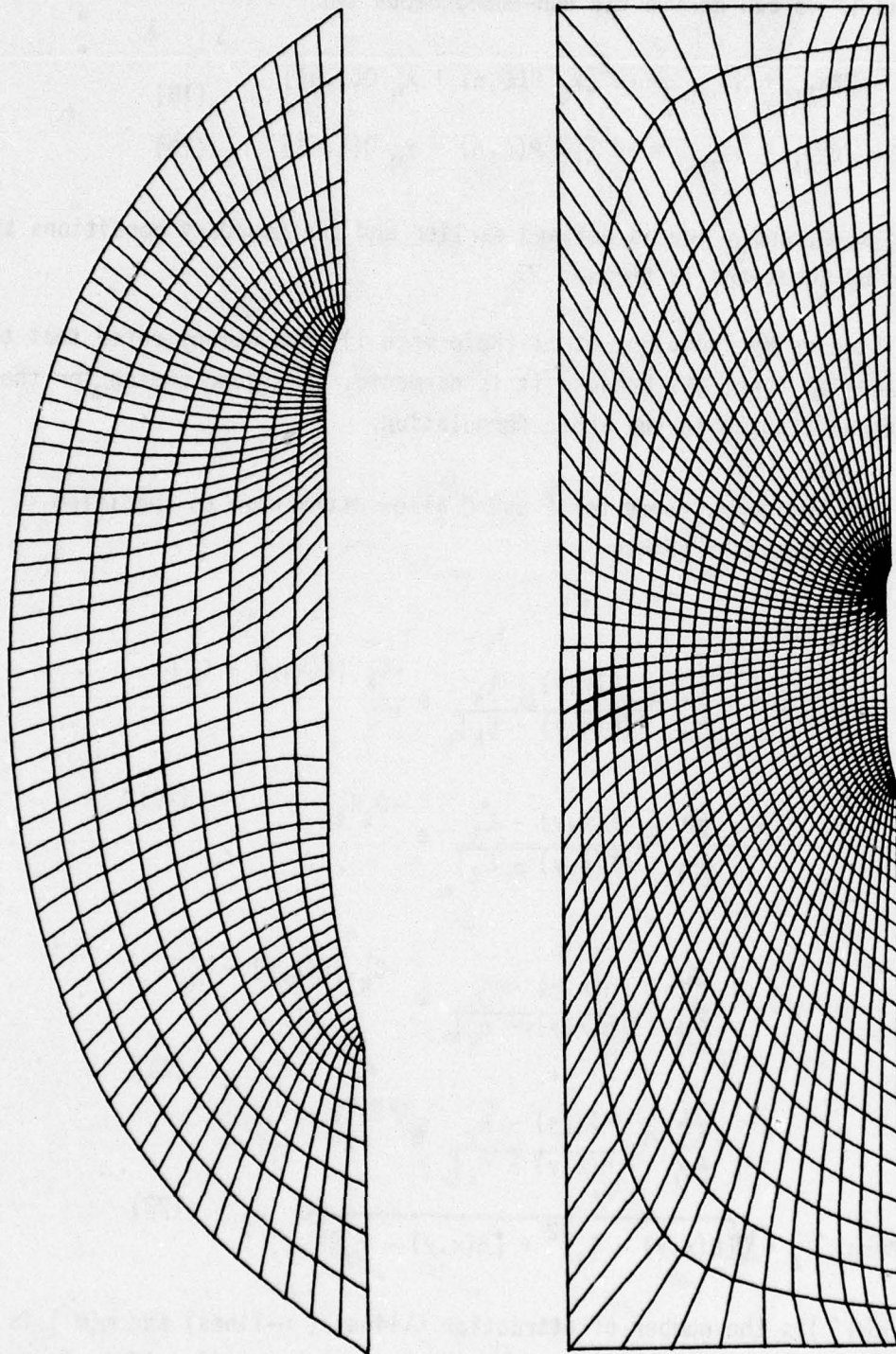
Figure 6. Agard AD HOC Study - NASA Forebody - 15° Boattail -
NASA Tunnel
Physical Coordinate System with No Contraction

By interchanging dependent and independent variables in Equations 16 and 17 we can derive the non-homogeneous set

$$\alpha x_{\xi\xi} - 2\beta x_{\xi\eta} + \gamma x_{\eta\eta} = -J^2[x_\xi \, P(\xi,\eta) + x_\eta \, Q(\xi,\eta)] \qquad (18)$$

$$\alpha y_{\xi\xi} - 2\beta y_{\xi\xi} + \gamma y_{\eta\eta} = -J^2[y_\xi \, P(\xi,\eta) + y_\eta \, Q(\xi,\eta)] \qquad (19)$$

where α, β, and γ are as defined earlier and the boundary conditions are given by Equations 12 through 15.

Studies by Thompson, et al (Reference 1) have demonstrated that the exponential function, because it is harmonic, is a good choice for the functions P and Q in the above formulation.

The following forms for P and Q allow attraction to specified ξ and η-lines and/or points.

$$P(\xi,\eta) = -\sum_{k=1}^{n} A_k \frac{\xi(x,y) - \xi_k}{|\xi(x,y) - \xi_k|} \; e^{-C_k \, |\xi(x,y) - \xi_k|}$$

$$-\sum_{\ell=1}^{m} B_\ell \frac{\xi(x,y) - \xi_\ell}{|\xi(x,y) - \xi_\ell|} \; e^{-D_\ell R_\ell} \qquad (20)$$

$$Q(\xi,\eta) = -\sum_{k=1}^{n'} A_k' \frac{\eta(x,y) - \eta_k}{|\eta(x,y) - \eta_k|} \; e^{-C_k' \, |\eta(x,y) - \eta_k|} \qquad (21)$$

$$-\sum_{\ell=1}^{m'} B_\ell' \frac{\eta(x,y) - \eta_\ell}{|\eta(x,y) - \eta_\ell|} \; e^{-D_\ell' R_\ell}$$

$$(22)$$

where $R_\ell = \sqrt{[\xi(x,y) - \xi_\ell]^2 + [\eta(x,y) - \eta_\ell]^2}$,

and $n(n')$ is the number of attraction ξ-lines (η-lines) and $m(m')$ is the number of attraction ξ-points (η-points). Note that $\xi(x,y) \neq \xi_k, \xi_\ell$ and

$\eta(x,y) \neq \eta_k, \eta_\ell$. The first term of Equation 20 has the effect of attracting the ξ-lines to the ξ_k-lines. The second term of Equation 20 causes the attraction of ξ-lines to the points $[\xi_\ell, \eta_\ell]$. Similar results are obtained with the two parts of Equation 21 with the η-lines to the η_k-lines and the points $[\xi_\ell, \eta_\ell]$.

The attraction concept is a useful tool; however, its application requires trial and error for the beginner and experience in order to quickly obtain a suitable coordinate system.

The above method of attraction was found to work well when it is desirous to attract to the $\xi_k=1$ or the $\eta_k=1$ lines only. The method was also suitable for contraction to a line in the field. However, when it was found to be necessary to attract to the $\eta_k=\eta_{max}$ line in addition to the $\eta_k=1$ line, the results were often erratic. This attraction to both boundaries was found to be necessary to prevent the grid size at the outer boundary from becoming larger than 1.0, for example, in the case where large amounts of contraction were desired at the body ($\eta_k=1$) boundary. Instead of holding the grid spacing nearly constant at the outer boundary, all of the η-lines tended to collapse away from the outer boundary and locate in the bottom part of the field near the area of high attraction.

In an attempt to cure the problem, the forms of P and Q have been re-defined as

$$P(\xi,\eta) = \sum_{k=1}^{n} A_k\ e^{-C_k|\xi(x,y) - \xi_k|} + \sum_{\ell=1}^{m} B_\ell\ e^{-D_\ell R_\ell} \quad (23)$$

$$Q(\xi,\eta) = \sum_{k=1}^{n'} A'_k\ e^{-C'_k|\eta(x,y) - \eta_k|} + \sum_{\ell=1}^{m'} B'_\ell\ e^{-D'_\ell R_\ell} \quad (24)$$

where R_ℓ is still defined by Equation 22. This modification was developed jointly by the author and Hodge (Equation 22). The coefficients are as defined for Equations 20 and 21. For attraction to a line or point at $\eta=1$

13

(or $\xi=1$), the A_k's and B_ℓ's should be negative. This ensures that P and Q are negative in the area of the lower (i.e., ξ or $\eta=1$) boundary. For attraction to an upper boundary ($\xi=\xi_{max}$ or $\eta=\eta_{max}$) the attraction coefficients should be positive.

Equation 23 is different from Equation 20 in sign and the deletion of the $(\xi(x,y) - \xi_k)/|\xi(x,y) - \xi_k|$ term which is a SIGN function. It has been determined that this SIGN function was the cause of the erratic behavior discussed earlier. Equation 24 was changed in a similar manner.

Figures 7 and 8 are plots of the solution of Equations 18 and 19 with P and Q defined by Equations 23 and 24. The coefficients for P and Q are listed in Tables 1 and 2 for Figures 7 and 8, respectively. The resulting grids are obviously more suitable to numerical calculation. The grid spacing has been adjusted to account for the flow gradients in the velocity potential flow solution described in Section III. The boundary conditions can be applied on coordinate lines which are coincident with the boundaries. These two coordinate systems have been used successfully to solve for the velocity potential for flows which are totally subsonic.

3. OPTIMIZING THE COORDINATE GENERATION

In general, the convergence rate for the numerical solution of a partial differential equation solved on an orthogonal grid is faster than one solved on a non-orthogonal grid. With an orthogonal grid, the coefficients of the off-diagonal terms are minimized. With this in mind, several attempts have been made to make the grid system more orthogonal by altering the equation set 18, 19, and 12 through 15.

The first procedure merely involved changing the boundary conditions on Γ_2^* and Γ_4^* from Dirichlet to Neumann expressions. The requirement for orthogonality from Equations 18 and 19 is

$$\beta = x_\xi x_\eta + y_\xi y_\eta \equiv 0 \qquad (25)$$
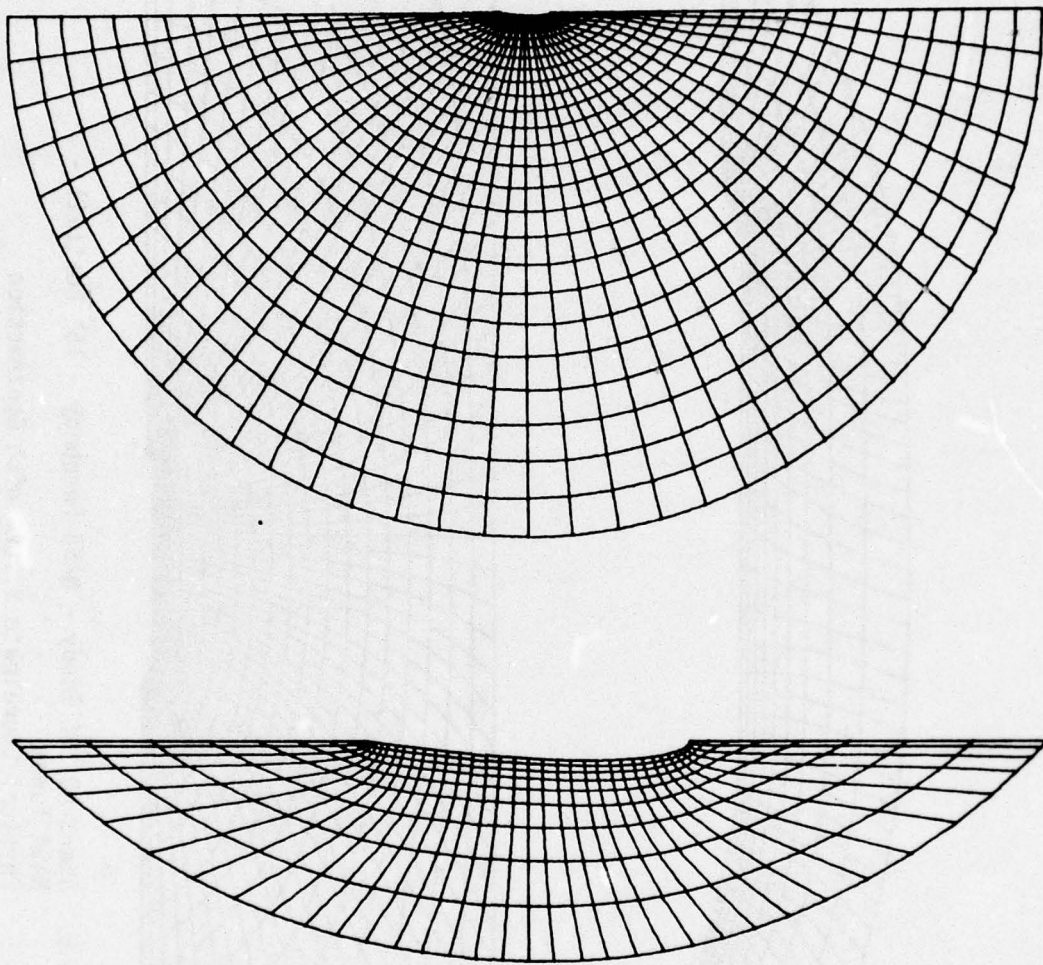
Figure 7.   NACA 0012 Airfoil - Physical Coordinate System with
Contraction
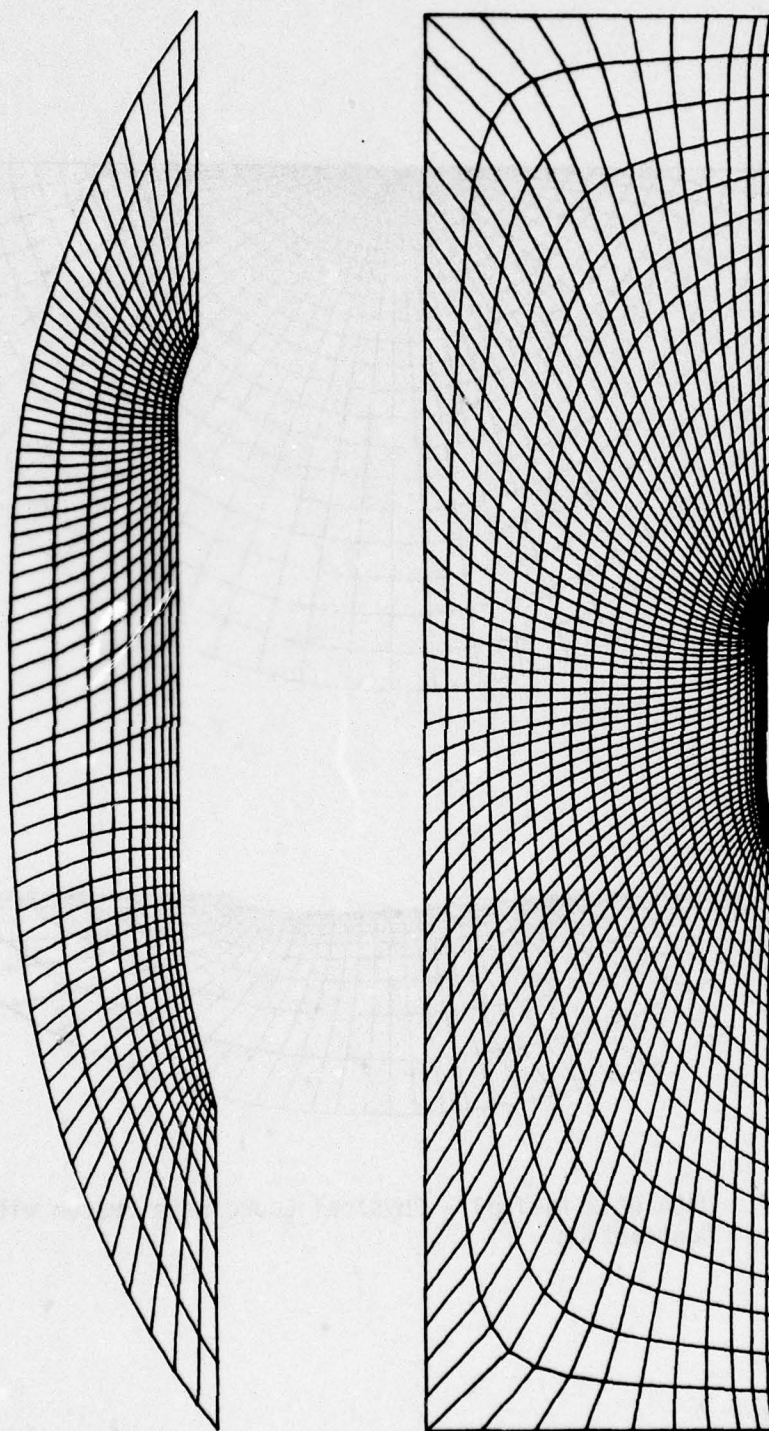
Figure 8. Agard AD HOC Study - NASA Forebody - 15° Boattail -
NASA Tunnel
Physical Coordinate System with Contraction

TABLE I
COEFFICIENTS OF P AND Q EQUATIONS FOR NACA 0012
AIRFOIL (Figure 7)   IMAX=37, JMAX=30

COEFFICIENTS OF EQ. 23

ξ_k	A_k	C_k	ζ_ℓ	η_ℓ	B_ℓ	D_ℓ
			1	1-20	-5.	1.0
			2		-5.	
			36	↓	+5.	
			37		+5.	
			1	1-10	-400.	
			2		-200.	
			36		+200.	
			37	↓	+400.	↓

COEFFICIENTS OF EQ. 24

η_k	A'_k	C'_k	ξ_ℓ	η_ℓ	B'_ℓ	D'_ℓ
1	-300.	1.0				
2	-250.					
3	-200.					
4	-150.					
5	-100.					
6	-50.					
20	+0.05					
21						
22						
23						
24						
25						
26						
27						
28						
29	↓	↓				
30						

TABLE 2
COEFFICIENTS OF P AND Q EQUATIONS FOR THE AGARD AD HOC
STUDY 15° BOATTAIL BODY (Figure 8)   IMAX=61, JMAX=25

COEFFICIENTS OF EQ. 23

ξ_k	A_k	C_k	ξ_ℓ	η_ℓ	B_ℓ	D_ℓ
1	-100.	1.0	1	1-10	-100.	1.0
2	-100.	↓	2		-50.	
60	+100.		60	↓	+50.	↓
61	+100.	↓	61	↓	+100.	↓

COEFFICIENTS OF EQ. 24

η_k	A'_k	C'_k	ξ_ℓ	η_ℓ	B'_ℓ	D'_ℓ
1	-600.	1.0	20	8-14	+1.0	1.0
2			21			
3	↓		22			
4	-500.		23			
5	-400.		24			
6	-300.		25	↓		
7	-200.		20	48-54		
8	-100.		21			
15	+0.08		22			
16			23			
17			24			
18			25	↓	↓	↓
19						
20						
21						
22						
23						
24						
25	↓	↓				

18

Along Γ_2^* and Γ_4^*, $y_\eta = 0$ for the physical coordinate systems illustrated thus far. Therefore, Equation 25 reduces to

$$x_\xi x_\eta = 0$$

However, as $x_\eta \neq 0$, we must have $x_\xi = 0$. Therefore, the new boundary conditions for Γ_2^* and Γ_4^* are as follows:

$$\begin{bmatrix} x_\xi \\ y \end{bmatrix} = \begin{bmatrix} 0 \\ g_2(\xi_2, \eta) \end{bmatrix} \quad , \quad [\xi, \eta] \; \epsilon \; \Gamma_2^* \tag{26}$$

$$\begin{bmatrix} x_\xi \\ y \end{bmatrix} = \begin{bmatrix} 0 \\ k_2(\xi_4, \eta) \end{bmatrix} \quad , \quad [\xi, \eta] \; \epsilon \; \Gamma_4^* \tag{27}$$

Figure 9 is a solution of the equation set 18, 19, 12, 26, 14, and 27. For the first iterate, x must still be specified along Γ_2^* and Γ_4^*. For all iterations after the first one, the value of x is calculated from a one-sided second-order difference expression. As explained by Thames (Reference 2), the use of Dirichlet boundary conditions with Equations 16 and 17 guarantees that the solution satisfies the maximum principle, which, in turn, guarantees that all extrema occur on the boundaries of region D. However, with the use of the Neumann boundary condition shown in Equations 26 and 27, the above is no longer the case. The problem which can result is illustrated in Figure 10, which is an enlargement of the rear portion of the body of Figure 9. The points $(1,2)$ and $(\xi_{MAX}, 2)$ both are outside the boundaries specified by Γ_1. This problem was solved by applying the boundary conditions of Equations 26 and 27 at each individual point on Γ_2^* and Γ_4^* only as long as the x-distance between points did not become less than a specified input value. The results of such a requirement are illustrated in Figures 11 and 12, where the smallest step size allowed was 0.005 and 0.00375, respectively. Obviously, the Neumann boundary condition is not valid at the points where the minimum step size was enforced, but the results are still excellent.

Figure 9. Agard AD HOC Study - NASA Forebody - 15° Boattail -
NASA Tunnel
Physical Coordinate System with Contraction and
Neumann Boundary System

Maximum Principle Not Satisfied
(Cross-Over Within Field)

Figure 10. Enlargement of AFT Portion of Coordinate System
of Figure 9

Figure 11. NACA 0012 Airfoil - Physical Coordinate System with
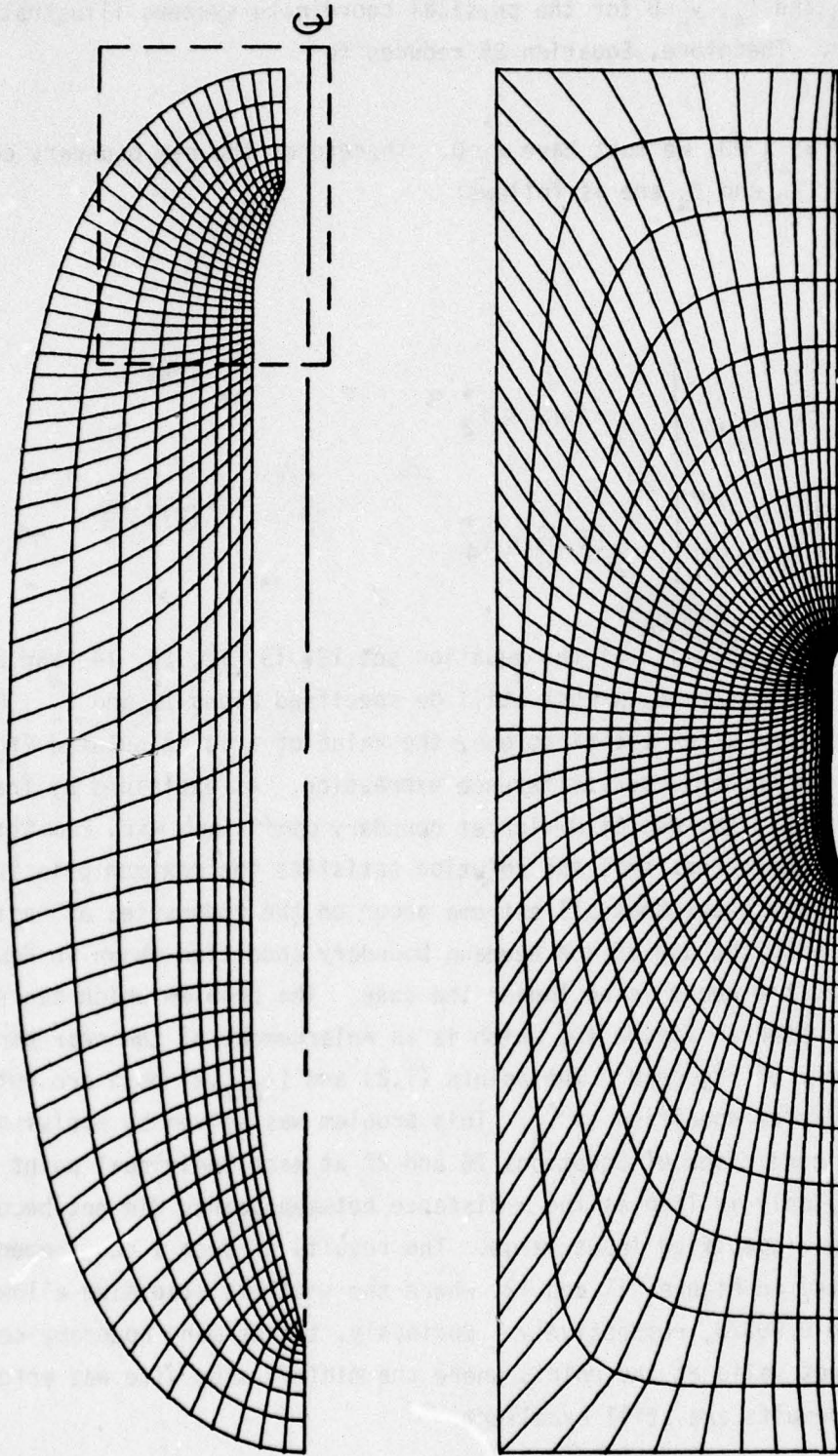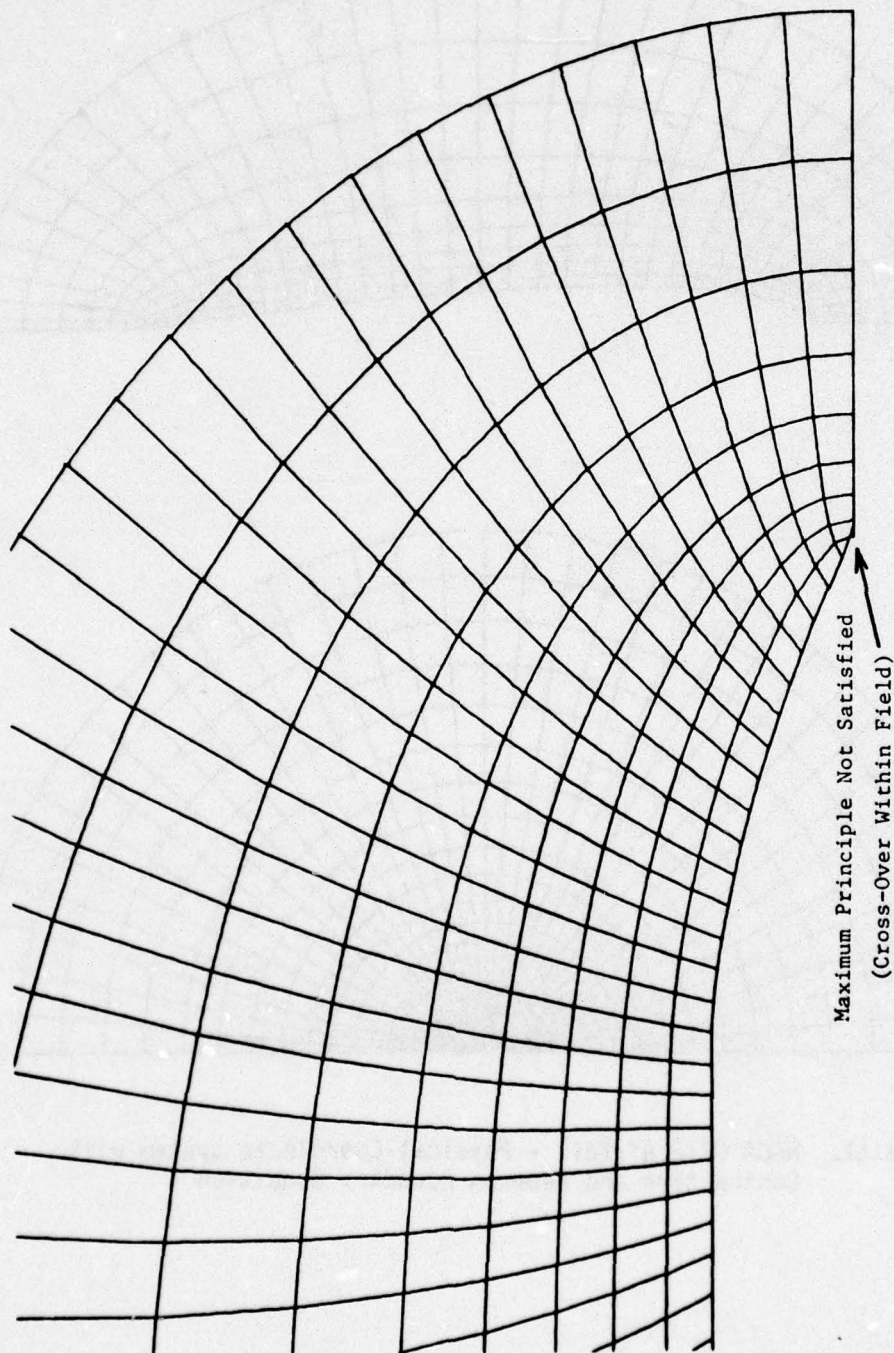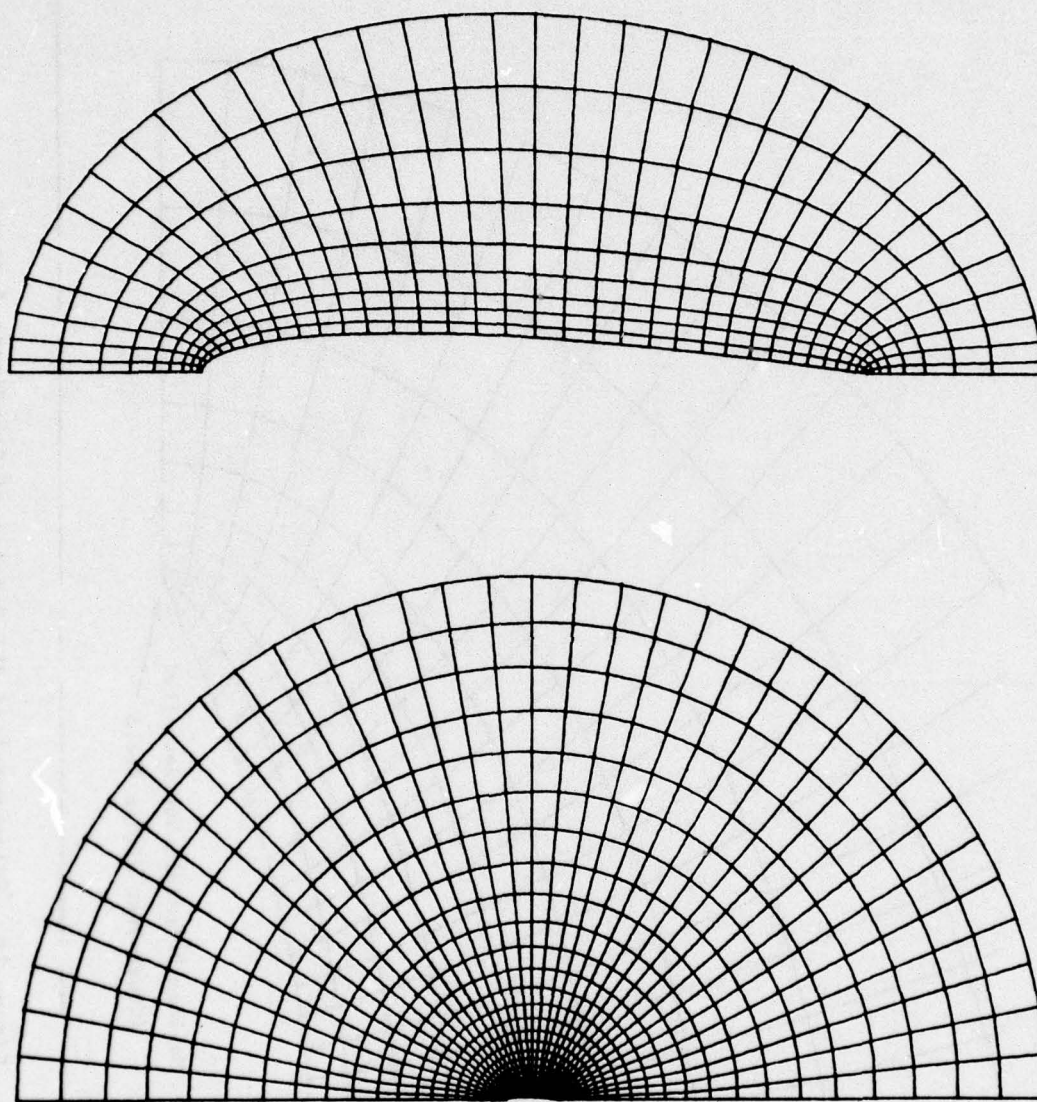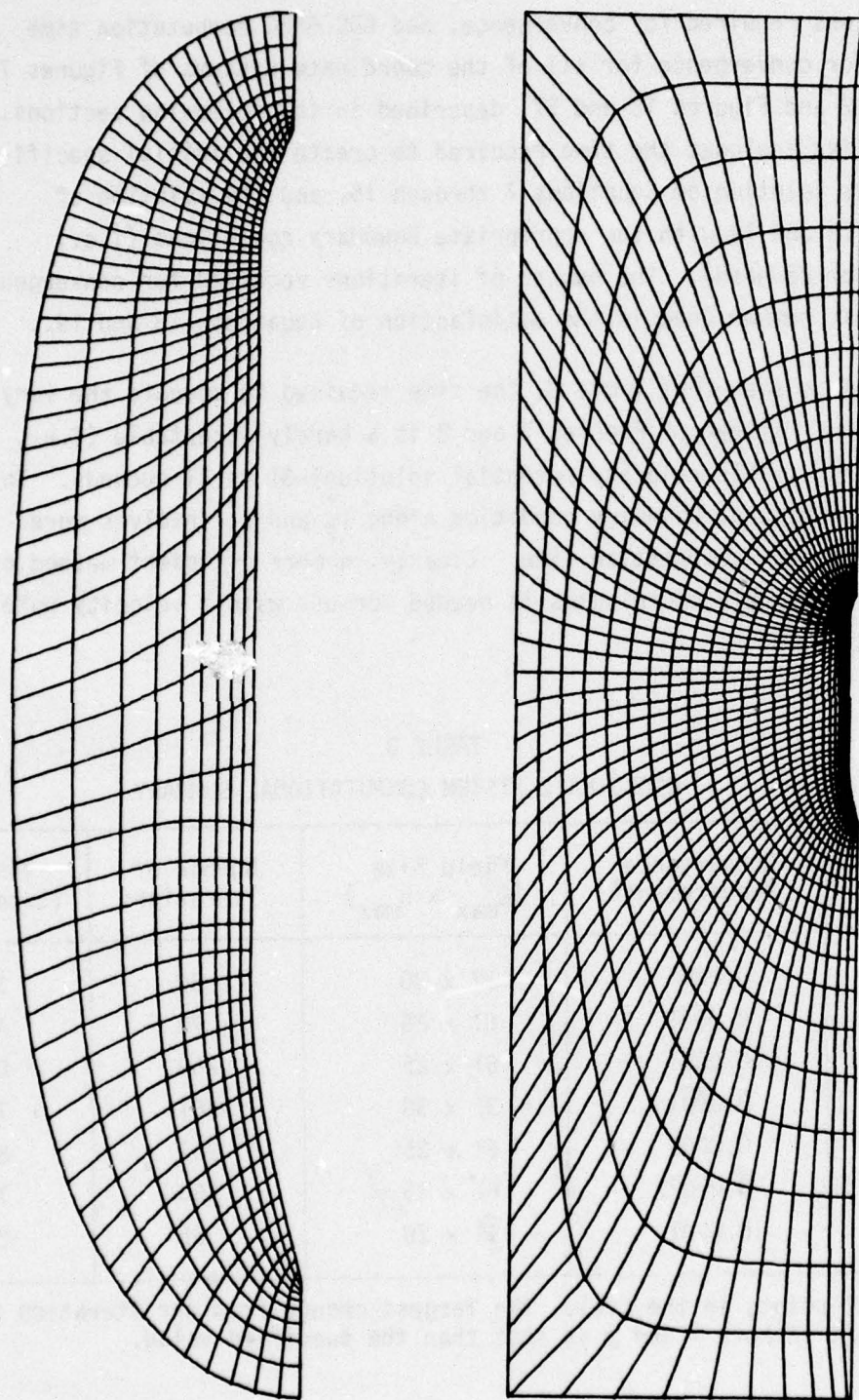Contraction and Neumann Boundary Condition

Figure 12. Agard AD HOC Study - NASA Forebody - 15° Boattail -
NASA Tunnel
Physical Coordinate System with Contraction and
Controlled Neumann Boundary Condition

Table 3 is a list of the convergence requirements, field size, number of iterations required for convergence, and CDC 6600 computation time required for convergence for all of the coordinate systems of Figures 7 through 12 and Figures 15 and 17, described in the following sections. The data list includes the time required to create the initial specification, the solution of Equations 7 through 15, and the solution of Equations 18 and 19 with the appropriate boundary conditions (i.e., Dirichlet or Neumann). The number of iterations required for convergence is only that number used in the satisfaction of Equations 18 and 19.

As can be seen from Table 3, the time required to compute the very non-orthogonal system of Figures 7 and 8 is a barely acceptable (i.e., for the compressible velocity potential solution) 31 to 41 seconds. To apply the orthogonal boundary condition along Γ_2^* and Γ_4^* involves more than doubling the computation time. Clearly, a more efficient method of producing acceptable coordinates is needed for use with a velocity potential solution.

TABLE 3

COORDINATE SYSTEM COMPUTATIONAL SUMMARY

Figure Number	Convergence Requirement*	Field Size $(\xi_{max} \times \eta_{max})$	Number of Iterations	Time (Seconds)
7	0.0001	37 x 30	80	31
8	0.0001	61 x 25	72	41
9	0.0001	61 x 25	259	83
11	0.0001	37 x 30	351	73
12	0.0001	61 x 25	257	84
15	0.00027	81 x 15	350	75
17	0.0001	111 x 20	65	23

*For all points in the field, the largest change from one iteration to the next in both x and y is less than the specified value.

4. DEVELOPMENT OF A STREAMLINE TYPE COORDINATE SYSTEM

The coordinate systems developed in Subsection C are very useful for the solution of the velocity potential equation as long as the flow is totally subsonic (i.e., the equation type is elliptical). As the flow becomes supersonic the equation type is hyperbolic and one-side upwind differences must be employed for computational stability. The problem with the coordinate systems discussed until now is that "upwind" is not readily evident. This problem will be discussed fully in Section III.

One solution to the problem is the introduction of a streamline type of coordinate system. Figure 13 illustrates the new system. The system is mainly oriented toward the "wind-tunnel" type of boundaries. With this system the η=constant lines are obviously in the streamline direction and allow the easy application of one-sided upwind derivatives for the flow solution.

Figure 14 is the initial specification of the ogive-cylinder-boat-tail body of Figure 12. In Figure 14, a new initial specification method was used which was suggested by Ghia (Reference 3). The method has not yet been adapted to the coordinate system of Figure 1. (For future references, the coordinate system of Figure 1 will be referred to as the "elliptical" type of coordinate system and that of Figure 14 as the "streamline" type). Figure 15 represents the best coordinate system found with this procedure. Figure 16 is a plot of $P(\xi,\eta)$ used in the calculation. Neumann boundary conditions were applied on Γ_2, Γ_3, and Γ_4. This coordinate system was used to solve problems which had supersonic "pockets" in the boattail area with good success. However, as can be seen from Table 3, the 72.7 sec computation time for the creation of the coordinate system was unacceptable.

25

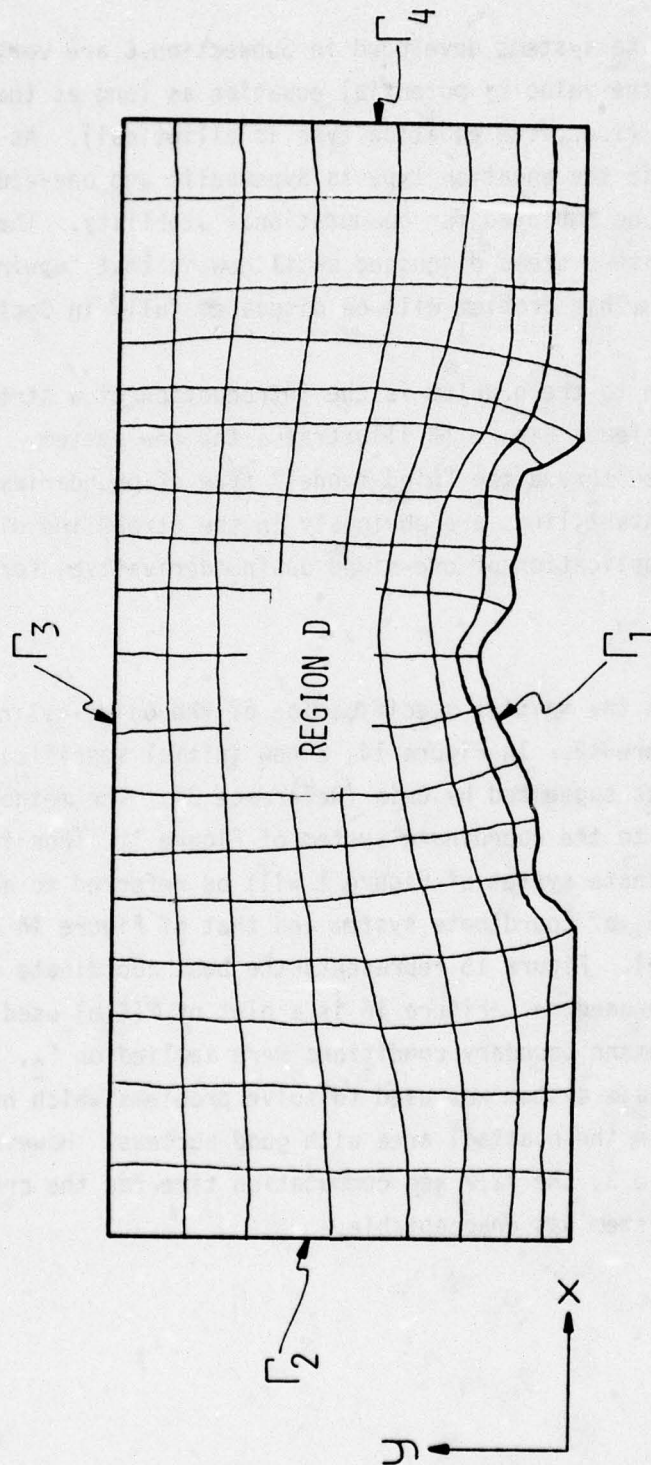Figure 13. "Streamline" Type Physical Plane (Natural Body-fitted Coordinates)
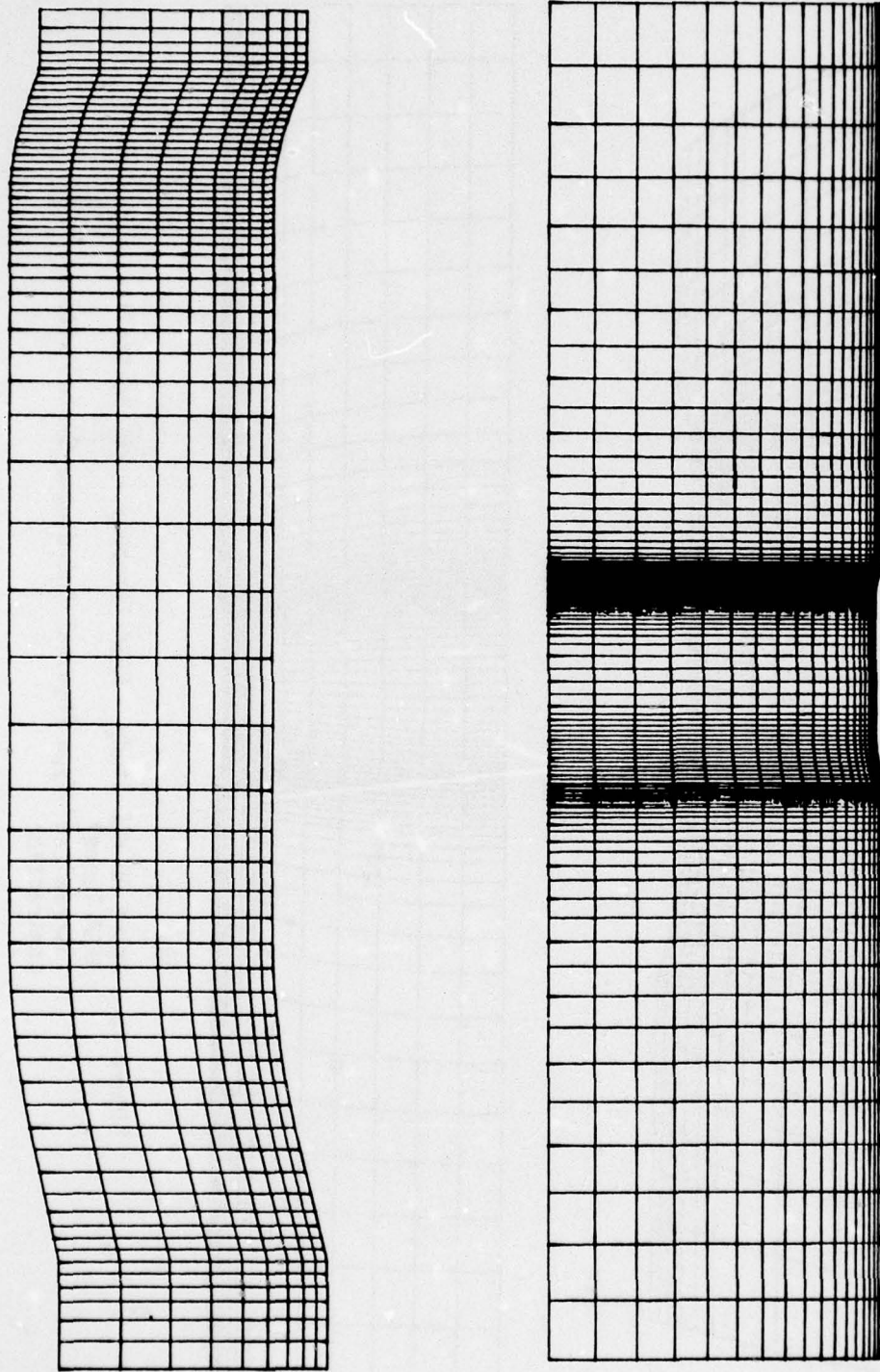
Figure 14. Agard AD HOC Study - NASA Forebody - 15° Boattail - NASA Tunnel "Streamline" Type Physical Coordinates System Initial Specification
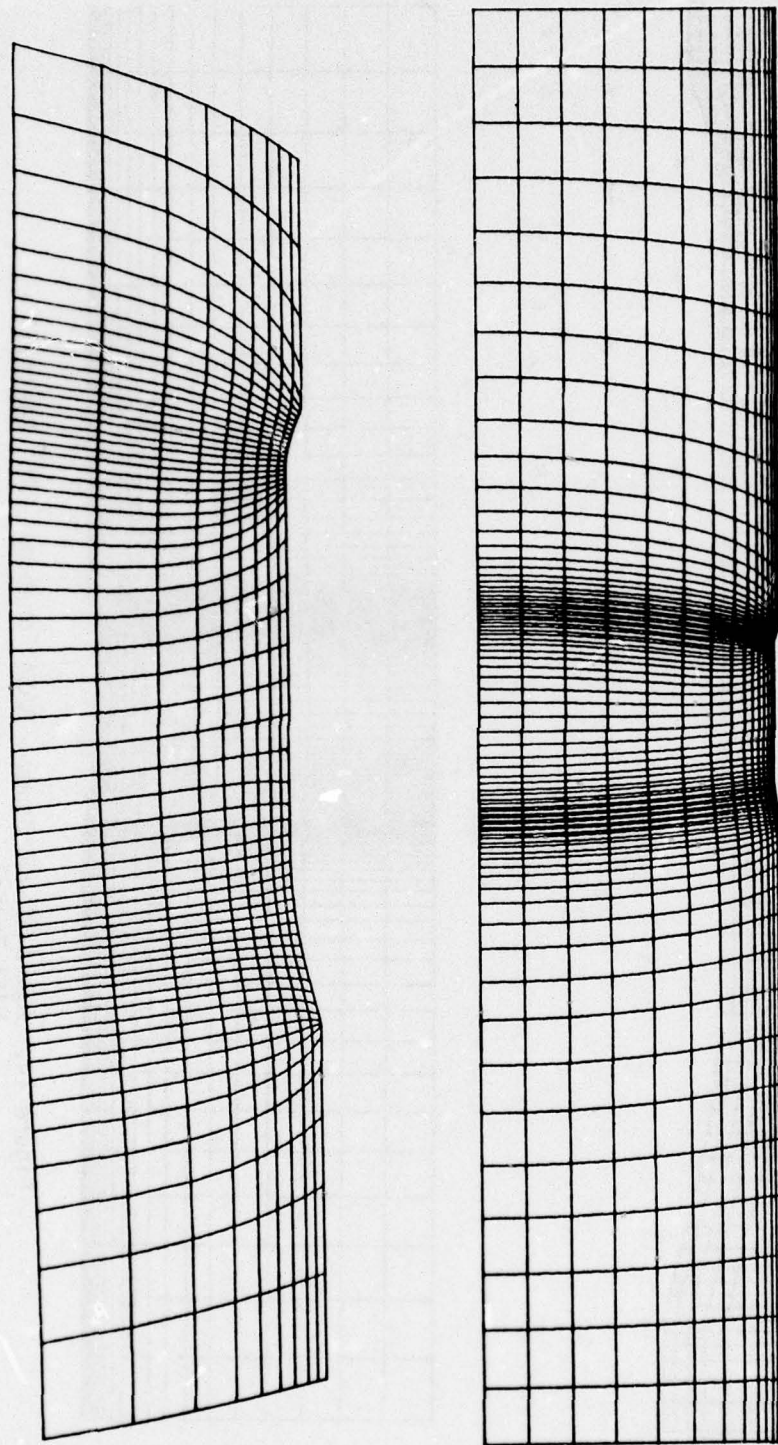
Figure 15. Agard AD HOC Study - NASA Forebody - 15° Boattail - NASA Tunnel "Streamline" Type Physical Coordinate System with Contraction
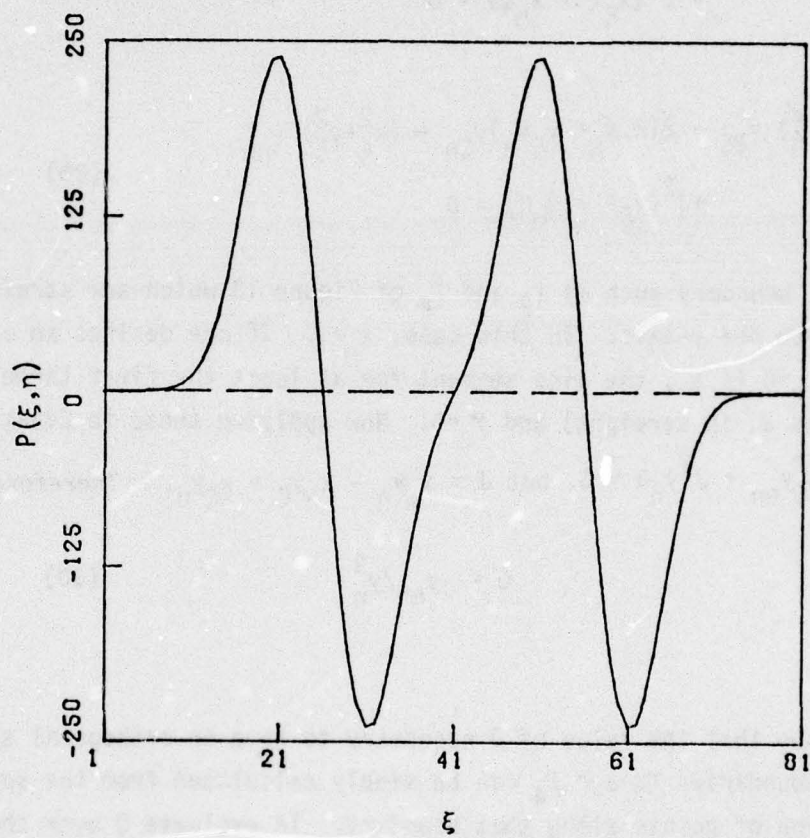
Figure 16. P - Distribution Applied to Figure 15

To solve this computation time problem and to achieve more orthogonal systems, the following method suggested by Ghia (Reference 3) was implemented. Consider writing Equations 18 and 19 as

$$(x_\eta^2 + y_\eta^2) \, x_{\xi\xi} - 2(x_\xi x_\eta + y_\xi y_\eta) x_{\xi\eta} + (x_\xi^2 + y_\xi^2) \, x_{\eta\eta}$$
$$+ \, J^2 (x_\xi P + x_\eta Q) = 0 \tag{28}$$

and

$$(x_\eta^2 + y_\eta^2) \, y_{\xi\xi} - 2(x_\xi x_\eta + y_\xi y_\eta) y_{\xi\eta} + (x_\xi^2 + y_\xi^2) \, y_{\eta\eta}$$
$$+ J^2 (y_\xi P + y_\eta Q) = 0 \tag{29}$$

Consider a boundary such as Γ_2 and Γ_4 of Figure 13 which are straight and aligned with the y-axis. In this case, $x_\eta = 0$. If one desires an orthogonal system, $y_{\xi\xi} = 0$ (i.e., the line segment for at least the first three points, $\xi = 1$, 2, and 3, is straight) and $y_\xi = 0$. Now applying these to Equation 29, we find $x_\xi^2 y_{\eta\eta} + J^2 y_\eta Q = 0$, but $J = x_\xi y_\eta - x_\eta y_\xi = x_\xi y_\eta$. Therefore,

$$Q = -y_{\eta\eta}/y_\eta^3 \tag{30}$$

Which states that the value of Q necessary to have an orthogonal system near the boundaries Γ_2 and Γ_4 can be simply calculated from the specified distribution of points along that boundary. To evaluate Q over the interior of the field, make a linear distribution of Q between the two boundaries for each η-line, i.e.,

$$Q(\xi,\eta) = Q(\xi_{MAX},\eta) - \left[Q(\xi_{MAX},\eta) - Q(1,\eta) \right] \left[\frac{\xi_{MAX} - \xi}{\xi_{MAX} - 1} \right] \tag{31}$$

30

Equation 30 has been found to be easily applied and very effective. If a third order polynomial is used to specify the initial distribution of y along Γ_2 and Γ_4, the four coefficients of the polynomial can be determined by specifying y, y_η, and $y_{\eta\eta}$ at $\eta=1$ (the lower boundary) and y at $\eta=\eta_{max}$ (the upper boundary). Normally, $y_{\eta\eta}$ is chosen to be zero and y_η is the desired step size at the lower boundary. The η-line distribution of Figure 17 is governed by Q determined from Equation 30. The input value of y_η at the lower boundary was 0.0095. The converged solution had an average step size of 0.0097 between the $\eta=1$ and $\eta=2$ lines.

An analogous equation can be derived from Equation 28 for the boundary Γ_3 of Figure 13 when it is straight and aligned with the x-axis, that is,

$$P = -x_{\xi\xi}/x_\xi^3 \tag{32}$$

At the upper boundary of Figure 17, P was determined from Equation 32.

An expression for P can be derived from Equation 28 for an arbitrary boundary such as Γ_1 of Figure 13. Assume that along this coordinate line ($\eta=1$) $x_{\eta\eta}=0$. This means that the ξ-lines are straight for the small segment $\eta=1,2,3$. As the end boundaries Γ_2 and Γ_4 are specified, $y_{\eta\eta}$ may be calculated at $\eta=1$ at each end ($\xi=1$ and $\xi=\xi_{max}$). The value is calculated by a second-order one-sided difference expression, since this is the value used in the numerical calculations and not the input value used in the polynomial discussed above. A linear distribution of $y_{\eta\eta}$ between $y_{\eta\eta}(1,1)$ and $y_{\eta\eta}(\xi_{max},1)$ is taken and held constant for the calculation of P. Similarly, y_η may be determined along Γ_1 from the specified values of y at the end points. Then $x_{\xi\xi}$, $y_{\xi\xi}$, x_ξ, and y_ξ may be calculated from central difference expressions from the input specifications of x and y along Γ_1. Since an orthogonal system is desired, and $\beta=0$ is the condition for orthogonality, x_η may be determined
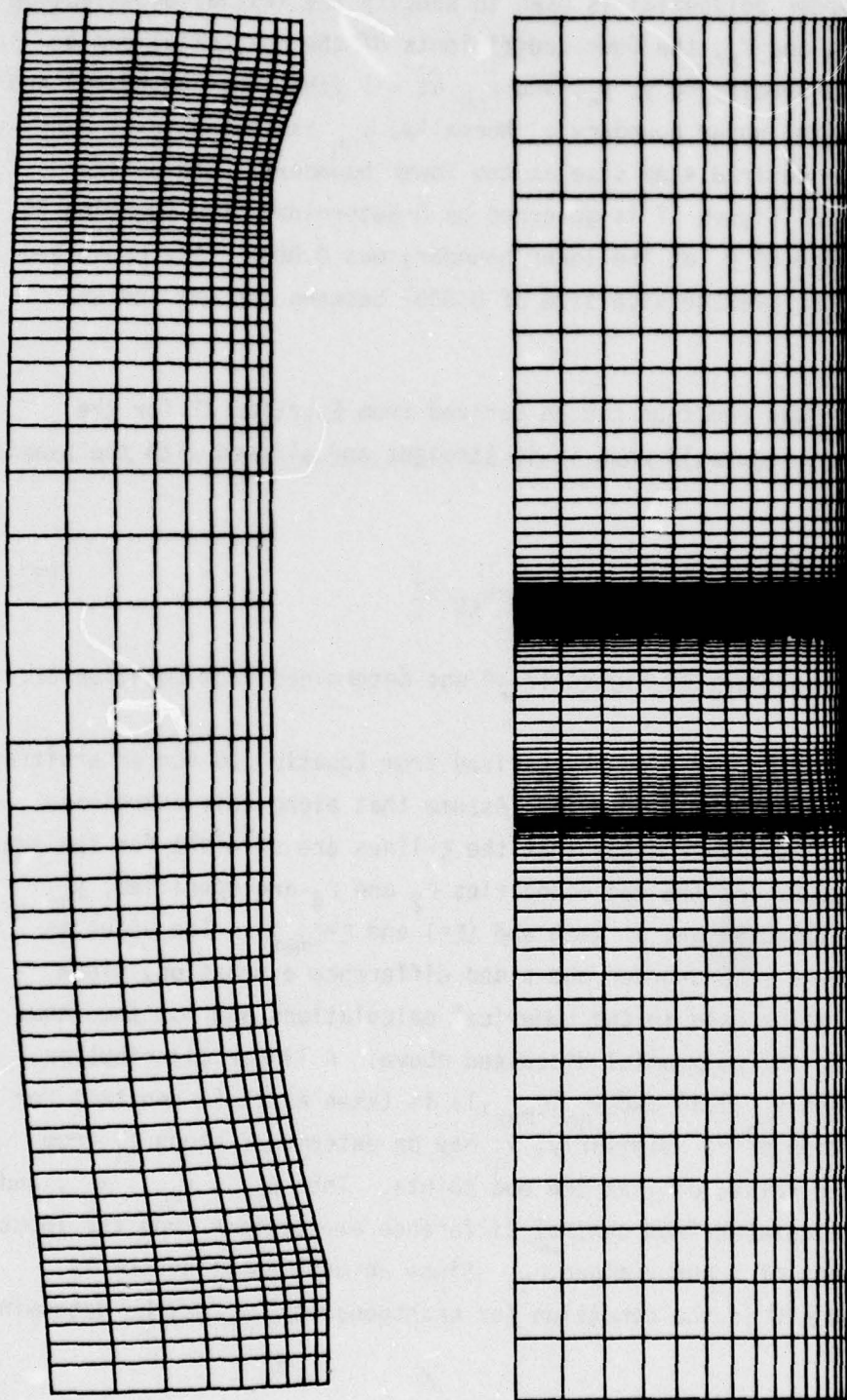
Figure 17. Agard AD HOC Study - NASA Forebody - 15° Boattail -
NASA Tunnel
"Streamline" Type Physical Coordinate System with
Calculated Contraction Factor

along Γ_1 from $\beta=0$, i.e., $x_\eta = -y_\xi y_\eta / x_\xi$. The Jacobian, $J=x_\xi y_\eta - x_\eta y_\xi$, is now known. Q is determined from Equation 30 at $\xi=1$ and $\xi=\xi_{max}$, and a linear distribution between the two values is taken. From the above assumption and now known values along Γ_1, the following equation can be applied:

$$P = - \frac{x_{\xi\xi}}{x_\xi J^2}(x_\eta^2 + y_\eta^2) - \frac{x_\eta}{x_\xi} Q \qquad (33)$$

The very successful results are shown in Figure 17. Because Q usually varies very rapidly in the vicinity of $\eta=1$, experience has shown that the Q used in Equation 33 should be an average of the values at $\eta=1$ and $\eta=2$.

Thompson (Reference 4) showed that a truncation error resulting in a numerical diffusive effect occurs in a flow calculation when the second derivatives of the physical coordinates ($x_{\xi\xi}$ in this case) are large in regions where the dependent variables have significant second derivatives in the direction normal to closely spaced coordinate lines. The use of the above method for determining P brought this problem to light. The method forces the grid spacing specified at the wall to be continued through the field. For example, large values of $x_{\xi\xi}$ at the wall forced the problem to propagate throughout the field. The result in the potential flow calculations was that the flow would not accelerate to the expected values in regions of large gradients in the flow direction. It was determined by trial and error and comparison with experimental and theoretical data that the condition

$$|x_{\xi\xi}| < 0.2|x_\xi| \qquad (34)$$

was sufficient to ensure minimum influence on the flow.

33

SECTION III

APPLICATION TO THE EXACT VELOCITY POTENTIAL EQUATION

The natural coordinate system method developed in Section II is applied to the numerical solution of the exact compressible velocity potential equation for two-dimensional and axisymmetric bodies in a simply connected field. The velocity potential equation is presented in cartesian form and then as it appears in the transformed plane. The boundary conditions are presented in both forms. The numerical method of solution is explained. The method of integrating the pressure distribution to obtain boattail drag on axisymmetric bodies is developed.

1. THE COMPRESSIBLE VELOCITY POTENTIAL EQUATION

For steady, invicid, irrotational, isentropic, compressible flow, the exact velocity potential equation in non-dimensional form is

$$A\phi_{xx} + B\phi_{xy} + C\phi_{yy} + D\phi_y = 0 \tag{35}$$

where the coefficients are defined as

$$A = a^2 - \phi_x^2 \tag{36a}$$

$$B = -2\phi_x\phi_y \tag{36b}$$

$$C = a^2 - \phi_y^2 \tag{36c}$$

$$D = \alpha a^2/y \tag{36d}$$

Two-dimensional flow is represented when $\alpha=0$ and axisymmetric flow when $\alpha=1$. The local speed of sound, a, is defined as

$$a^2 = \left(\frac{\partial P}{\partial \rho}\right)_s = \frac{1}{M_\infty^2} + \frac{\gamma_a - 1}{2}\left(1 - \phi_x^2 - \phi_y^2\right) \tag{37}$$

Also, the flow velocities are

$$u = \phi_x \tag{38a}$$

$$v = \phi_y \tag{38b}$$

34

A variable of major interest in boattail performance calculations is the pressure coefficient and is defined from Liepman and Roshko (Reference 5) as

$$C_p = \frac{2}{\gamma_a M_\infty^2}\left[\left(\frac{2+(\gamma_a-1)M_\infty^2}{2+(\gamma_a-1)M^2}\right)^{\frac{\gamma_a}{\gamma_a-1}} -1\right] \tag{39}$$

The transformation of the above equations into the computational (ξ, η)-plane is a straightforward process with the use of Thames' (Reference 2) thesis. Equation 35 becomes

$$k_1\phi_{\xi\xi} + k_2\phi_{\xi\eta} + k_3\phi_{\eta\eta} + k_4\phi_\xi + k_5\phi_\eta = 0 \tag{40}$$

where

$$k_1 = Ay_\eta^2 - Bx_\eta y_\eta + Cx_\eta^2 \tag{41a}$$

$$k_2 = -[2Ay_\xi y_\eta - B(x_\xi y_\eta + x_\eta y_\xi) + 2x_\xi x_\eta] \tag{41b}$$

$$k_3 = Ay_\xi^2 - Bx_\xi y_\xi + Cx_\xi^2 \tag{41c}$$

$$k_4 = -\frac{1}{J}[A(A_1 x_\eta - A_2 y_\eta) + BB_1 + C(C_1 x_\eta - C_2 y_\eta) - J^2 Dx_\eta] \tag{41d}$$

$$k_5 = -\frac{1}{J}[A(A_2 y_\xi - A_1 x_\xi) + BB_2 + C(C_2 y_\xi - C_1 x_\xi) + J^2 Dx_\xi] \tag{41e}$$

and

$$A_1 = y_\eta^2 \, y_{\xi\xi} - 2y_\xi y_\eta y_{\xi\eta} + y_\xi^2 y_{\eta\eta} \tag{42a}$$

$$A_2 = y_\eta^2 x_{\xi\xi} - 2y_\xi y_\eta x_{\xi\eta} + y_\xi^2 x_{\eta\eta} \tag{42b}$$

$$B_1 = J(x_\xi y_{\eta\eta} - x_\eta y_{\xi\eta}) + (x_\eta y_\eta J_\xi - x_\xi y_\eta J_\eta) \tag{42c}$$

$$B_2 = J(x_\eta y_{\xi\xi} - x_\xi y_{\xi\eta}) + (x_\xi y_\xi J_\eta - x_\eta y_\xi J_\xi) \tag{42d}$$

$$C_1 = x_\eta^2 y_{\xi\xi} - 2x_\xi x_\eta y_{\xi\eta} + x_\xi^2 \, y_{\eta\eta} \tag{42e}$$

$$C_2 = x_\eta^2 \, x_{\xi\xi} - 2x_\xi x_\eta x_{\xi\eta} + x_\xi^2 x_{\eta\eta} \tag{42f}$$

Equation 37 transforms to

$$\phi_x = (y_\eta \phi_\xi - y_\xi \phi_\eta)/J \qquad (43a)$$

$$\phi_y = (x_\xi \phi_\eta - x_\eta \phi_\xi)/J \qquad (43b)$$

2. BOUNDARY CONDITIONS

Various boundary conditions are presented below which can be combined to solve a problem of choice.

a. Uniform-Stream Boundary

$$u = u_\infty \qquad (44a)$$

$$v = 0 \qquad (44b)$$

This condition is easily expressed as

$$\phi = x \qquad (45)$$

$$\text{if} \quad x^2 + y^2 \to \infty \qquad (46)$$

b. Solid Wall Boundary

$$u = u(x,y) \qquad (47a)$$

$$v = 0 \qquad (47b)$$

By utilizing Equation 43b, the transformed expression for this boundary condition is

$$\phi_\eta = x_\eta \phi_\xi / x_\xi \qquad (48)$$

c. Tangential Flow Boundary

$$\underline{v} \cdot \hat{n} = 0 \qquad (49)$$

where

$$\underline{v} = \phi_x \hat{i} + \phi_y \hat{j}$$

and

$$\hat{n}^{(\eta)} = (-y_\xi \hat{i} + x_\xi \hat{j})/\sqrt{\gamma} \qquad (50)$$

36

Equation 50 is the expression for the unit normal to a line of constant
η given by Thames (Reference 2). The performance of the dot product
indicated by Equation 49 results in the transformed expression

$$\phi_\eta = \beta\phi_\xi/\gamma \tag{51}$$

Note that Equation 51 reduces to Equation 48 along a constant
η-line which is straight and parallel to the x-axis (i.e., a boundary
where $y_\xi = 0$).

d. Stagnation Point

Generally, it would be desirous to impose a complete stagnation
condition (i.e., u=0,v=0) at the leading and trailing edges of bodies
such as the NACA 0012 airfoil discussed in Section II. However, an
attempted application of both conditions when dealing with the potential
equation results in an over specification of the boundary condition.
Therefore, the boundary condition that was used is

$$\underline{v} = u^*\hat{i} \tag{52}$$

It was found to be necessary to specify u* initially as u_∞ when
the flow was started from a uniform stream. The values of u* were
gradually reduced to zero as the solution was iterated. The transfor-
mation of Equation 52 results in the expression

$$\phi_\eta = (y_\eta\phi_\xi - Ju^*)/y_\xi \tag{53}$$

3. NUMERICAL METHOD

In 1970, Murman and Cole (Reference 6) and Murman and Krupp (Reference
7) demonstrated that it is necessary to use a mixed finite difference
scheme to solve the potential equation when the flowfield has regions
of subsonic and supersonic flow. In the subsonic (elliptic) regions,

37

central difference expressions are necessary to ensure numerical stability. However, in supersonic (hyperbolic) regions, one-sided upwind differences are necessary.

The implementation of this method in this report has been simple and straightforward. First, the appropriate boundary condition is solved along the constant $\xi=1$ line (Γ_2 boundary). For the "elliptical" type of coordinate system of Figure 1, the tangential flow boundary condition, Equation 51, is solved. Both an explicit method and an implicit tri-diagonal solver have been used successfully. For the "streamline" type of system in Figure 14, the uniform stream boundary condition, Equation 45, was implemented. The solution then marched to the $\xi=2$ line. For each point on the line the type of Equation 39 is determined from the characteristic equation of Equation 35

$$Ay_x^2 - By_x + C = 0 \tag{54}$$

Specifically, if

$B^2-4AC<0$ it is elliptic

$B^2-4AC=0$ it is parabolic

$B^2-4AC>0$ it is hyperbolic

Thames (Reference 2) demonstrated that this type of the differential equation is invariant under the coordinate transformation. A,B, and C are determined by using only central differences. When Equation 35 is either elliptic or parabolic, second order, central derivatives are used to determine the coefficients, Equations 40 and 42 and to express Equation 39. When the equation type is hyperbolic, first order, one-sided upwind (decreasing ξ) differences in the ξ-direction and second order, central differences in the η-direction are used to determine the coefficients and express Equation 39. The appropriate boundary conditions are expressed in a similar manner and the entire ξ-line is posed in tri-diagonal form. This method is essentially line SOR.

After each line is solved the solution is weighted with acceleration parameters which have different values for the elliptic region, the hyperbolic region, and the boundaries. The values of these parameters are discussed in Section IV.

Each ξ-line is solved in turn until the rear boundary, Γ_4, is reached. It is solved in the same fashion as the Γ_2 boundary. This method is then iterated over the field until the maximum change of the potential from one iteration to the next reaches some convergent criteria.

This method has worked well for subsonic free-stream flow having embedded supersonic pockets with mild shocks. Thus far, the maximum free-stream Mach number that has been successfully run is 0.99. The "elliptical" type of coordinate system does not work when a supersonic area falls in a portion of the grid where the η-lines are not well aligned with the flow.

4. AXISYMMETRIC PRESSURE DRAG INTEGRATION

An important result of an axisymmetric potential flow solution is the integrated pressure drag. From Figure 18, we can see that

$$\underline{P} = -P\hat{n}^{(\eta)} \tag{55}$$

where $\hat{n}^{(\eta)}$ is the unit normal defined outward toward increasing η by Equation 50. With an increment in arc length, $ds = \sqrt{(dx)^2 + (dy)^2}$, giving an increment in surface area, $dS = 2\pi y ds$, the drag increment is defined as

$$dD = (\underline{P} \cdot \hat{i}) dS \tag{56}$$

where $\hat{i}$ is a unit normal in the positive x-direction. By carrying out the operation indicated by Equation 56,

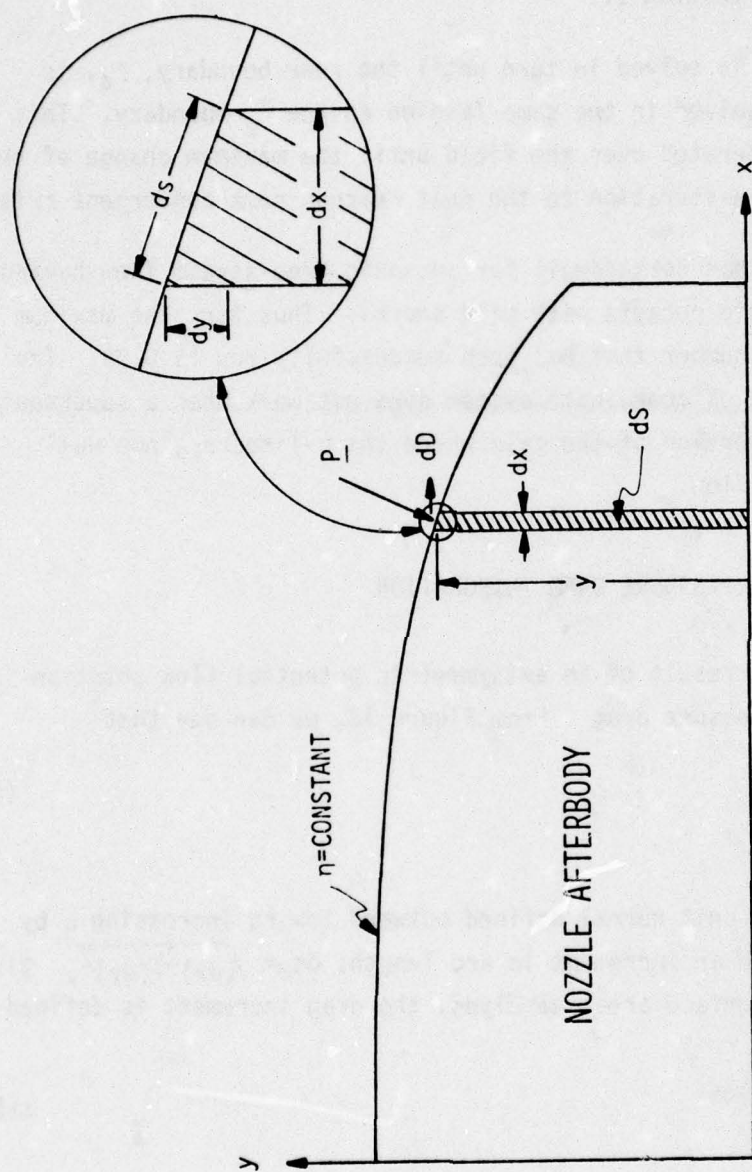$$dD = P y_\xi dS / \sqrt{\gamma} \tag{57}$$

39

Figure 18. Axisymmetric Body Pressure Drag Integration Diagram

40

Since the integration is along a line of constant η, $d\eta=0$. Therefore

$$ds=\sqrt{\gamma(d\xi)^2+2\beta d\xi d\eta+\alpha(d\eta)^2} \tag{58}$$

reduces to

$$ds = \sqrt{\gamma}\,d\xi \tag{59}$$

and Equation 57 becomes

$$dD=2\Pi yy_\xi P d\xi \tag{60}$$

By using the relation

$$C_p= \frac{P-P_\infty}{\frac{1}{2}\gamma_a P_\infty M_\infty^2} \tag{61}$$

we have

$$dD=\frac{1}{2}\gamma_a P_\infty M_\infty^2\, S_{ref}\, d(C_D) \tag{62}$$

So by equating Equations 60 and 61 and integrating, we get

$$C_D =\frac{2\Pi}{S_{ref}}\left[\frac{2}{\gamma_a M_\infty^2}\int_{\xi_1}^{\xi_2} yy_\xi d\xi \;+\; \int_{\xi_1}^{\xi_2} yy_\xi C_p d\xi\right] \tag{63}$$

where ξ_1 and ξ_2 are the starting and ending points, respectively, of the line integral over which the drag integration is desired. The first integral of Equation 63 is that part due to the reference pressure, P_∞, and should not be included in the normal definition of pressure drag. Therefore

$$C_D =\frac{2\Pi}{S_{ref}}\int_{\xi_1}^{\xi_2} yy_\xi C_p d\xi \tag{64}$$

The integral was accomplished numerically with the use of the integral formula

$$\int_{\xi_k}^{\xi_{k+1}} f(\xi)d\xi = [5f(\xi_k)+8f(\xi_{k+1})-f(\xi_{k+2})]/12 \tag{65}$$

Note that the normal inclusion of the step size, h, in the integration formula, Equation 65, is not necessary as $h=\Delta\xi=\Delta\eta\equiv1$ by definition when the coordinate transformation is applied. Such is the case in all difference formulas used in this report. To start and end the integration, the trapezoidal rule is used

$$\int_{\xi_k}^{\xi_{k+1}} f(\xi)d\xi=[f(\xi_k)+f(\xi_{k+1})]/2 \tag{66}$$

SECTION IV

CALCULATIONS

The velocity potential solution method discussed in Section III was
programmed in Fortran IV. In this section the basic capabilities and
limitations of the method are verified. The efficiency of the numerical
scheme and the effects of acceleration parameters are discussed. The
pressure drag integration method is demonstrated. Finally, the effects
of various boundary conditions on the flow over a cone-cylinder-boattail
are examined.

1. VERIFICATION

A sphere in an incompressible flow, a NACA 0012 airfoil at zero
angle of attack, an ogive-cylinder-boattail, and a parabolic arc body
of revolution were chosen for basic verification of the method.

Figure 19 shows pressure coefficient contours and local total
velocity contours for the sphere. From Karamcheti (Reference 8), the
minimum pressure coefficient on the body should be $C_p = -1.25$. The
calculated value of $C_p = -1.244$ is 0.48% in error. The calculated
maximum velocity on the body, $Q = 1.498$, is very close to the ideal value
of 1.500. The "elliptical" coordinate system used to calculate the
sphere flow was essentially a polar one with the far field at 15 body
diameters away.

Figure 20 illustrates the calculation for flow over a NACA 0012
airfoil at zero angle of attack. The data comparison for the incom-
pressible case is from Abbott and Von Doenhoff (Reference 9). The
M=0.63 and M=0.725 cases compare very well with the wind tunnel results
of References 9 and 10. The coordinate system used was that of Figure
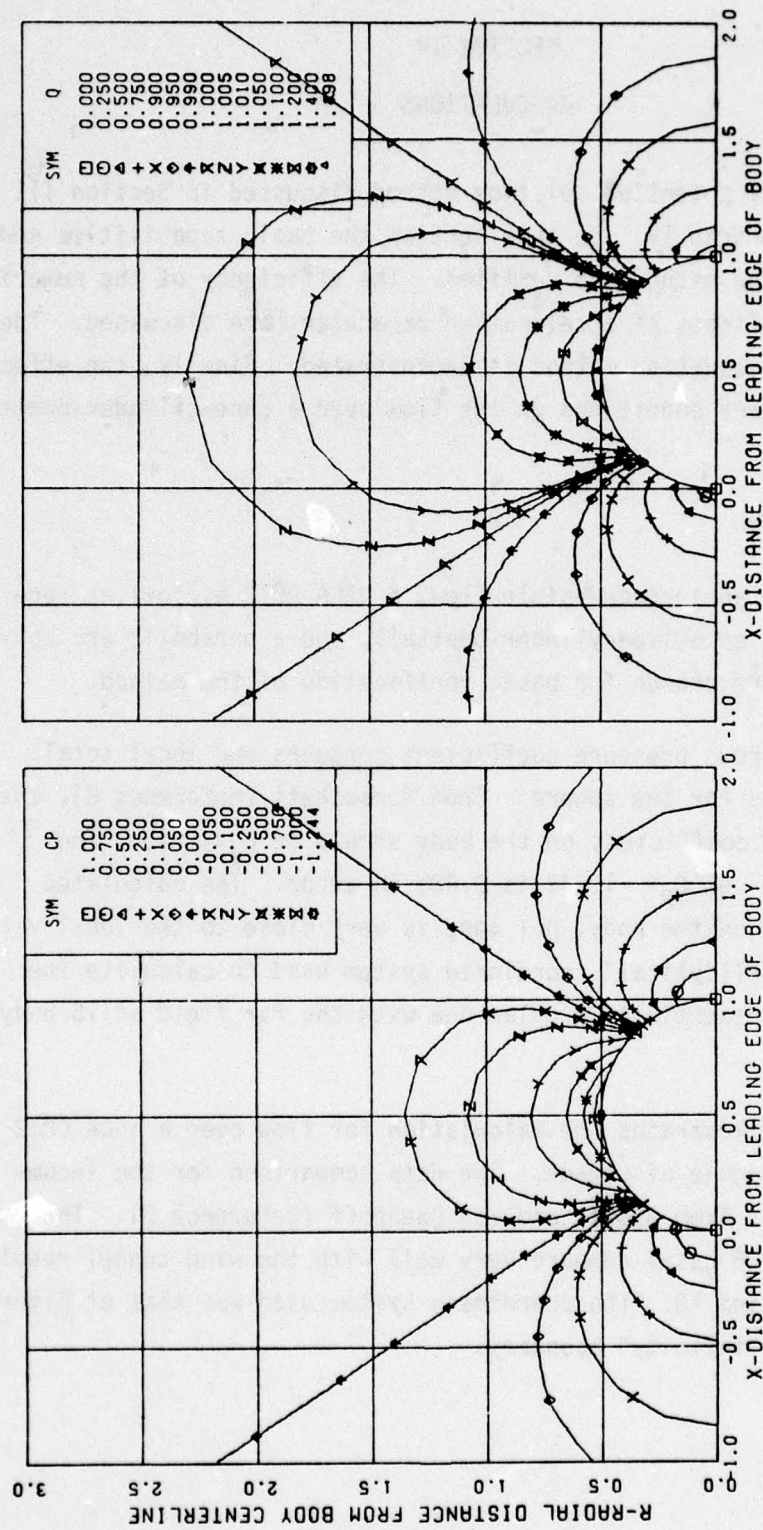11 which has an "infinity" boundary.

43

Figure 19. Contours of Constant Pressure Coefficient (CP) and
Local Total Velocity (Q) for Incompressible Flow
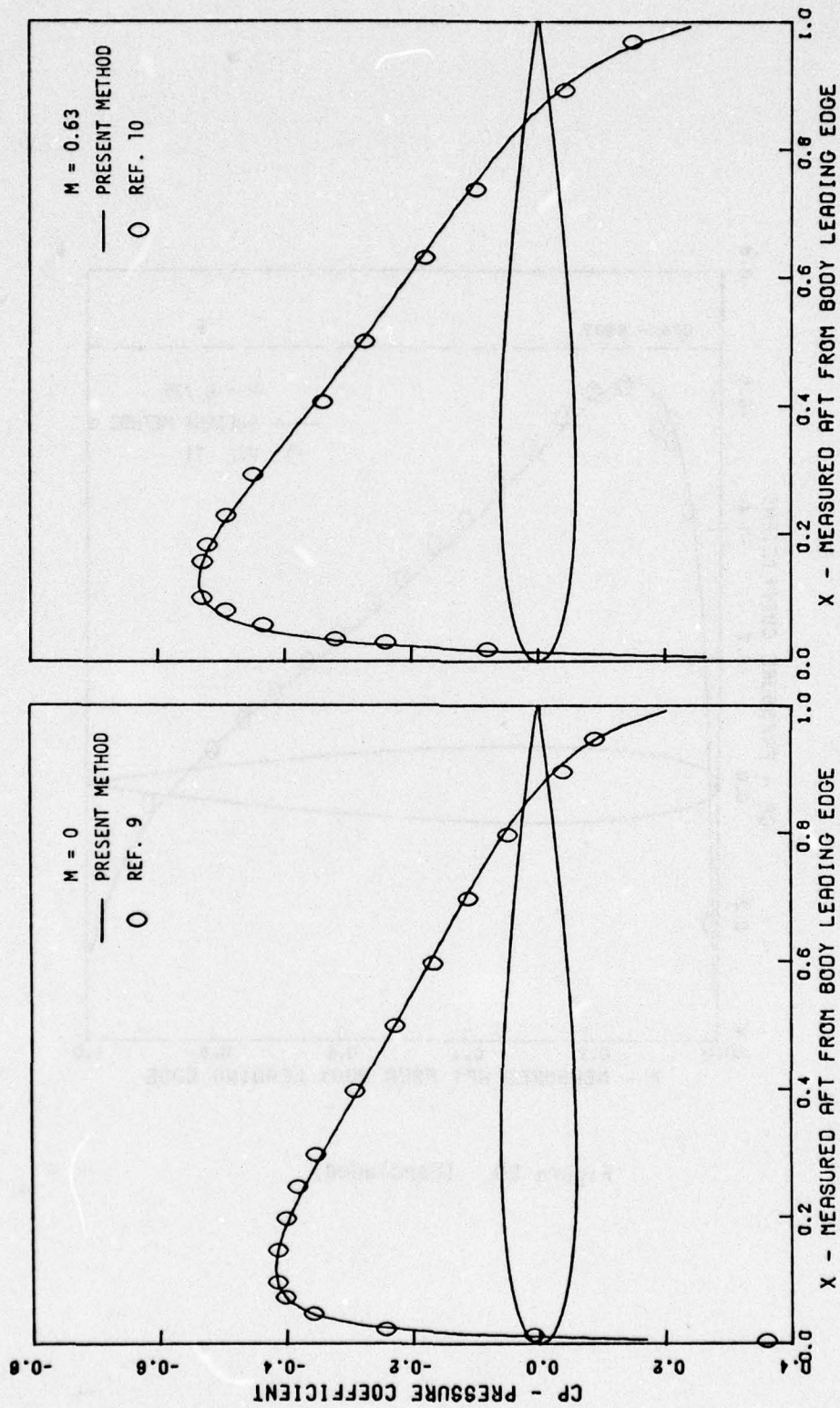Over a Sphere with an Infinity Boundary

Figure 20. Pressure Coefficient Distribution for Flow Over a
NACA 0012 Airfoil at Zero Angle of Attack for
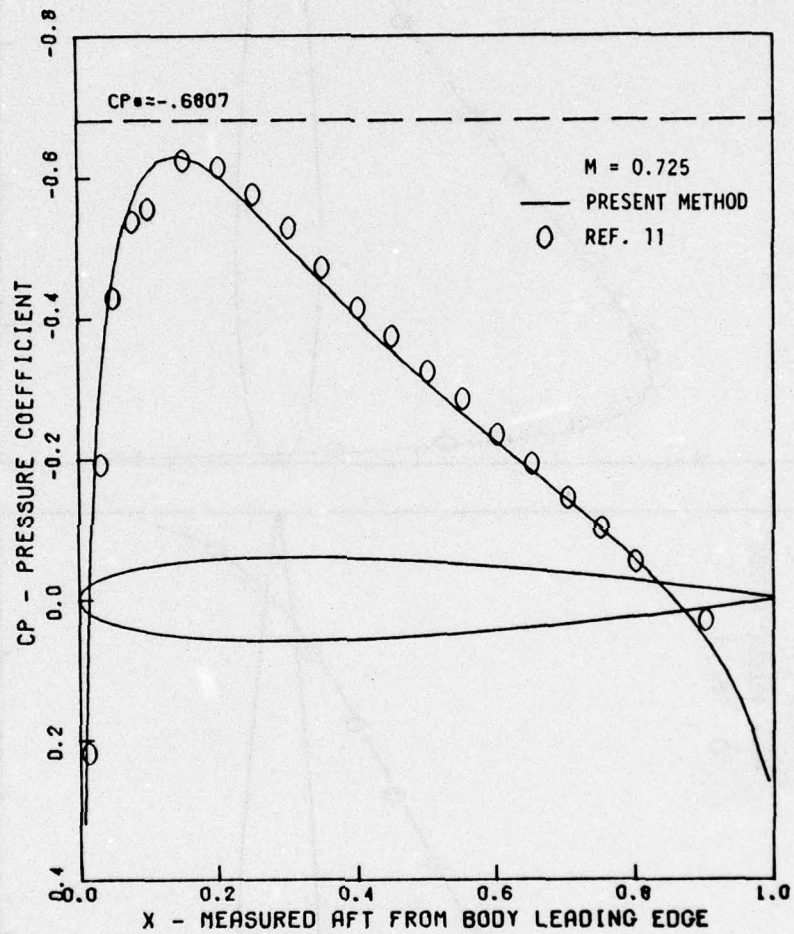Incompressible, M=0.63, and M=0.725 Far Field Flow
Conditions

Figure 20. (Concluded)

To check supercritical flowfield calculations, the body of Figure 17 was run at Mach numbers of 0.4, 0.6, 0.8, and 0.9. The results of Figure 21 show comparisons with wind-tunnel data from References 12 and 14 and the calculations of the Douglass-Neumann program (Reference 13). The results are quite good for all Mach numbers. The solution in the shock area in the M=0.9 case is very close to the experimental data. This is typical of non-conservative formulation of the governing equations. Figure 22 is a plot of the pressure distribution for the whole body. The symbols demonstrate the variable grid spacing typically used.

The coordinate system of Figure 17 represents the NASA LaRC 16T wind tunnel. The wall height was proportioned to 1.5 body lengths as reported by NASA LaRC (Reference 12). The wall boundary condition was simulated with a solid wall, Equation 48. The body was also run with the upper boundary placed at 5.0 body lengths away. With this configuration, the uniform-stream boundary condition, Equation 45, was implemented. For the range of Mach numbers considered, no appreciable effects of the upper boundary condition were seen. Because of the results of these calculations, it is felt that the solid-wall boundary condition is sufficient to represent the real LaRC 16T slotted wall for axisymmetric flows with only small supersonic pockets and when the body length to test section radius ratio is 1.0 or less.

To investigate flows near Mach 1.0, the 10% thick parabolic arc body of revolution tested by Taylor (Reference 15) was considered. The 80-inch model was tested in the NASA Ames 14-Foot Transonic Wind Tunnel. The wind tunnel has a square ventilated test section consisting of longitudinal slots with corrugated inserts. A turbulent boundary layer was induced on the model at R_{e_ℓ} =27 X 10^6. The data were not corrected for wall interference effects. The body was truncated at X/L=0.854 to permit mounting on the sting.
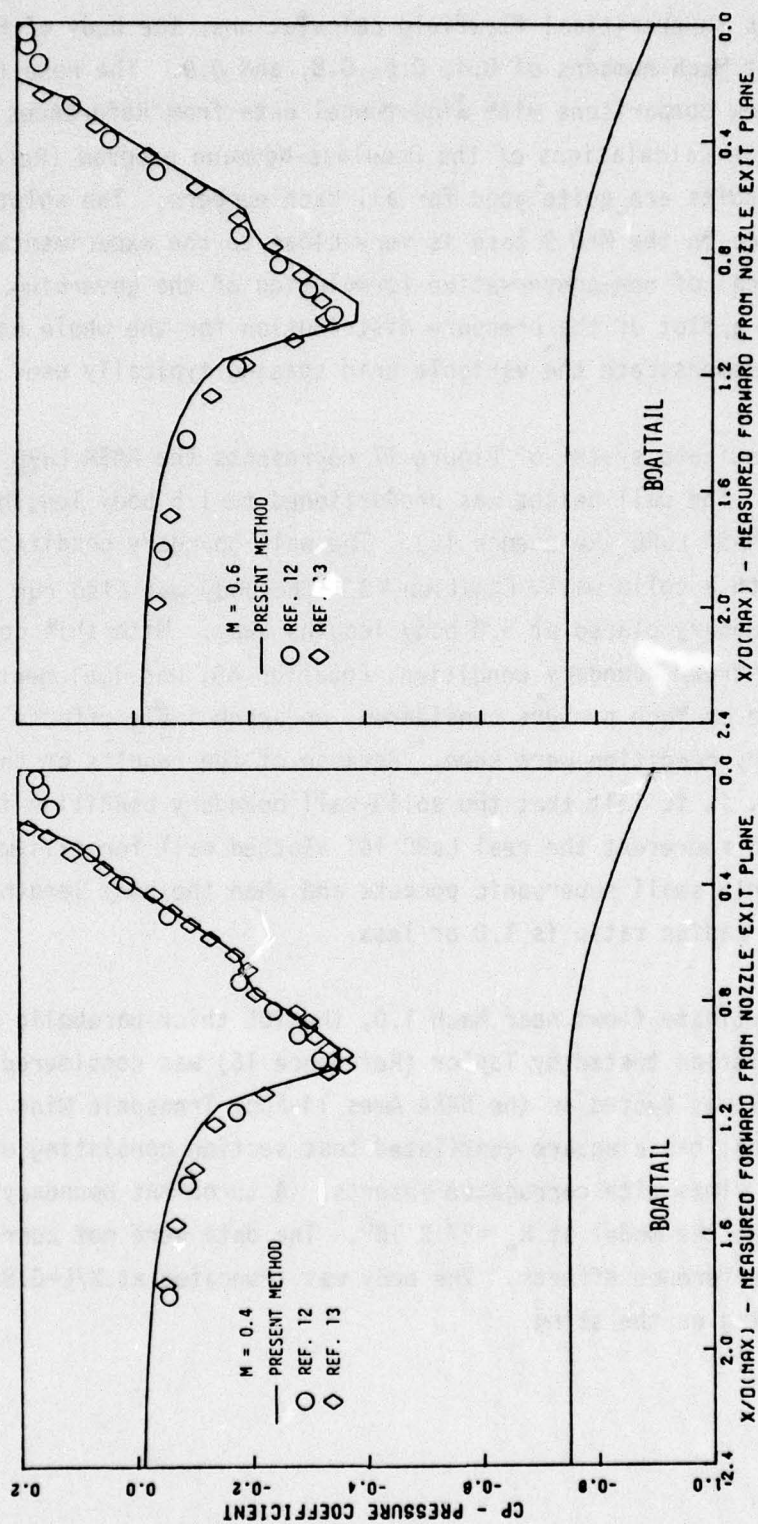
Figure 21. Pressure Distributions for Flow Over the Agard
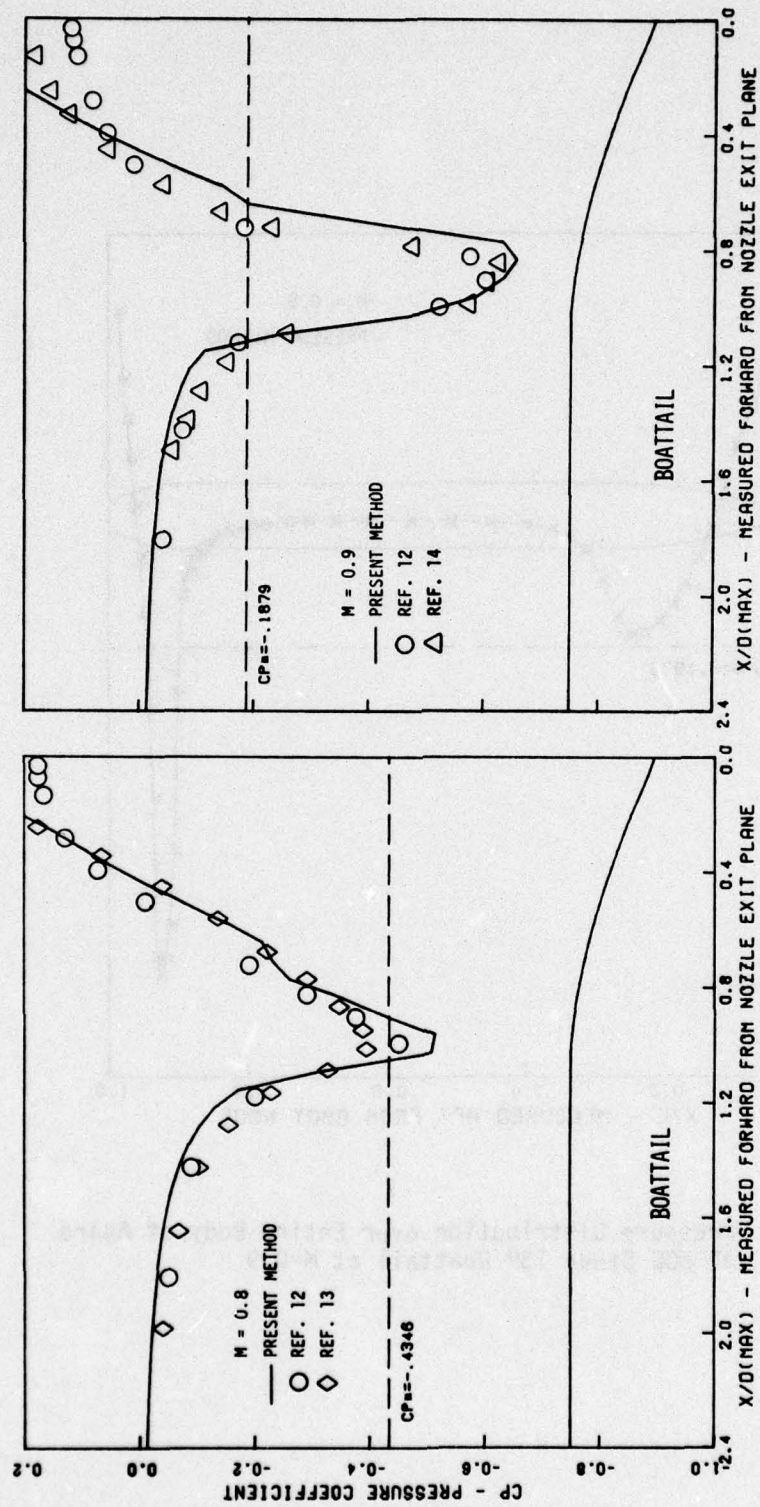AD HOC Study 150 Boattail for M=0.4, 0.6, 0.8, and 0.9
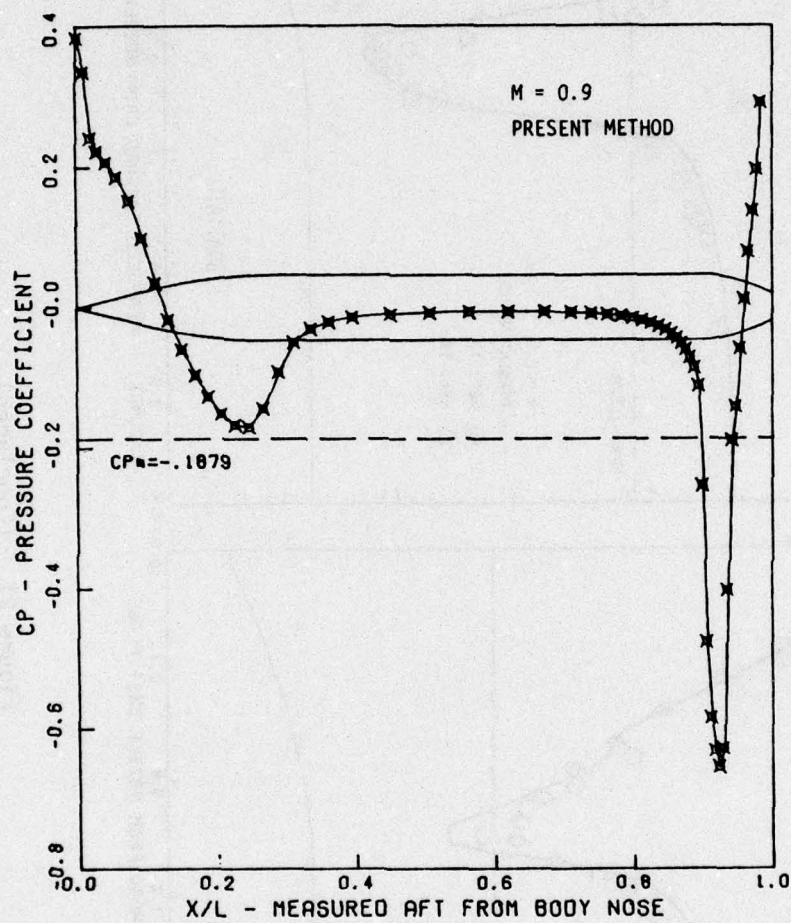
Figure 21. (Concluded)

Figure 22. Pressure Distribution over Entire Body of Agard
AD HOC Study 15⁰ Boattail at M=0.9

50

A calculation was made for this body at M=0.975. A solid wind-tunnel wall was placed at 1.0125 (81 inches) body lengths radius. The results of the calculation are shown in Figure 23. Also shown are the calculations of Bailey (Reference 16). The physical step size along the body was a constant 0.015 for $0.104 \leq X/L \leq 0.854$. Near the body nose the step size was reduced to 0.0065. As can be seen from Figure 23, the calculated solution over-shoots the experimental data and Bailey results over the first 15% of the body as if the nose were slightly blunted. Initially, this problem was thought to be caused by the selection of x-step size in nose area. Numerous variations of $x(\xi)$, $x'(\xi)$ and $x''(\xi)$ were tried in the nose area to study the grid selection effect on the solution in this area. The results were always the same. Refinement and smoothing of the grid merely resulted in better definition of the same solution.

Another possible source of the problem is the manner in which coordinate system ξ-derivatives (i.e., x_ξ, $x_{\xi\xi}$, y_ξ, $y_{\xi\xi}$,) are evaluated at the nose on the lower boundary. For the solution of Figure 23, second-order central derivatives are used. It would seem apparent that this procedure would have the effect of smoothing the discontinuity at the nose into a cusp with the expected effect of causing an under expansion in the nose area. However, as Figure 23 illustrates, this was not the case. Note that as the tangency condition, Equation 49, is solved along the lower boundary, Γ_1, and not the potential equation, Equation 39, the actual value of y at the nose point does not enter into the calculations. The solution along Γ_1 was also separately attempted with second-order upwind and downwind differences to evaluate the derivatives at the nose. In both cases, the solution diverged at the nose.

The calculated solution over the remainder of the body is in excellent agreement with the experimental data of Taylor (Reference 15). The solution converges well in all areas except in the shock region. In the 150 iterations allowed in the calculation, the maximum change in ϕ at the last iteration was 0.000012. Elsewhere in the field, the convergence was better than 0.0000005. The inflection in the pressure
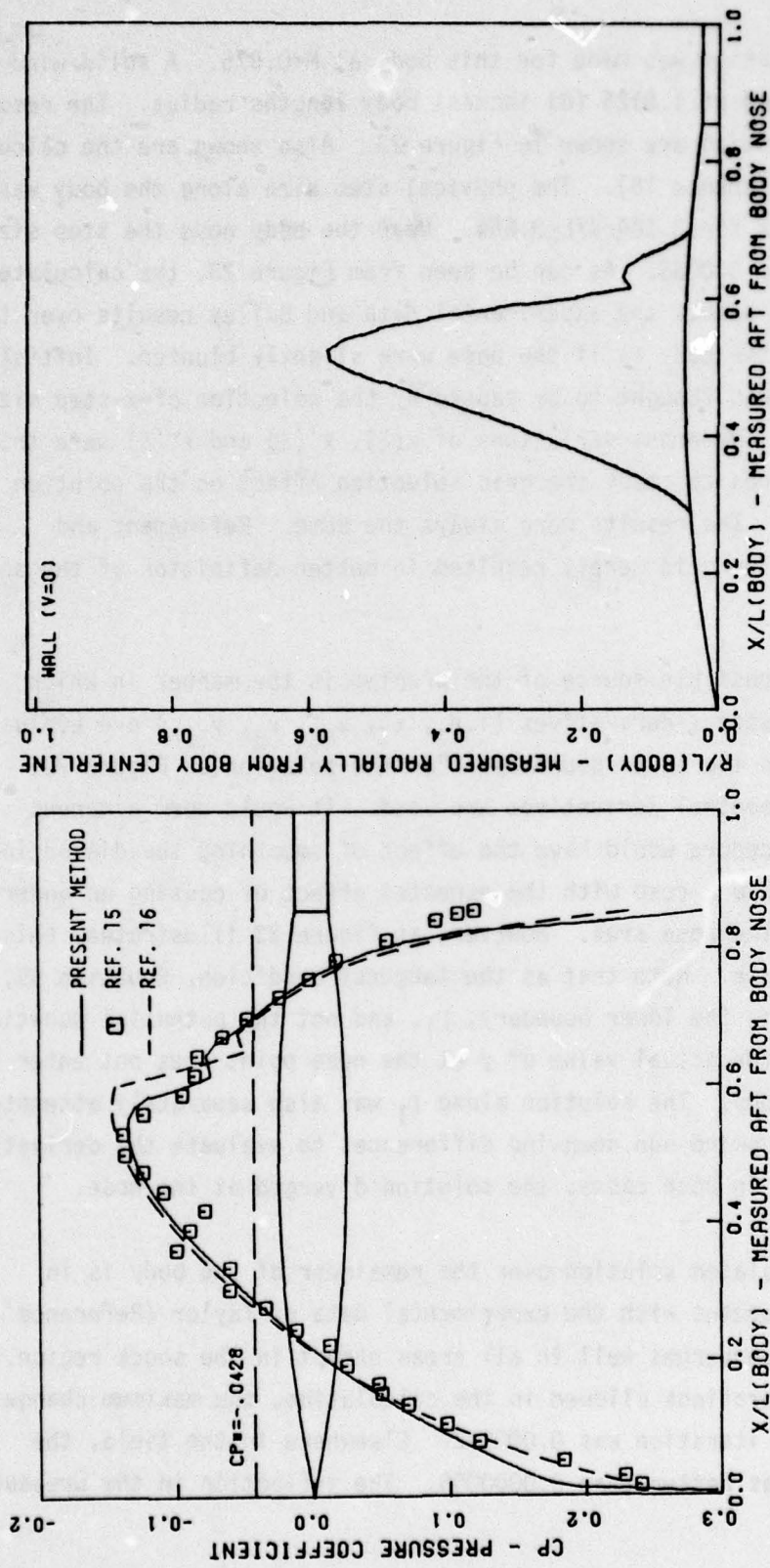
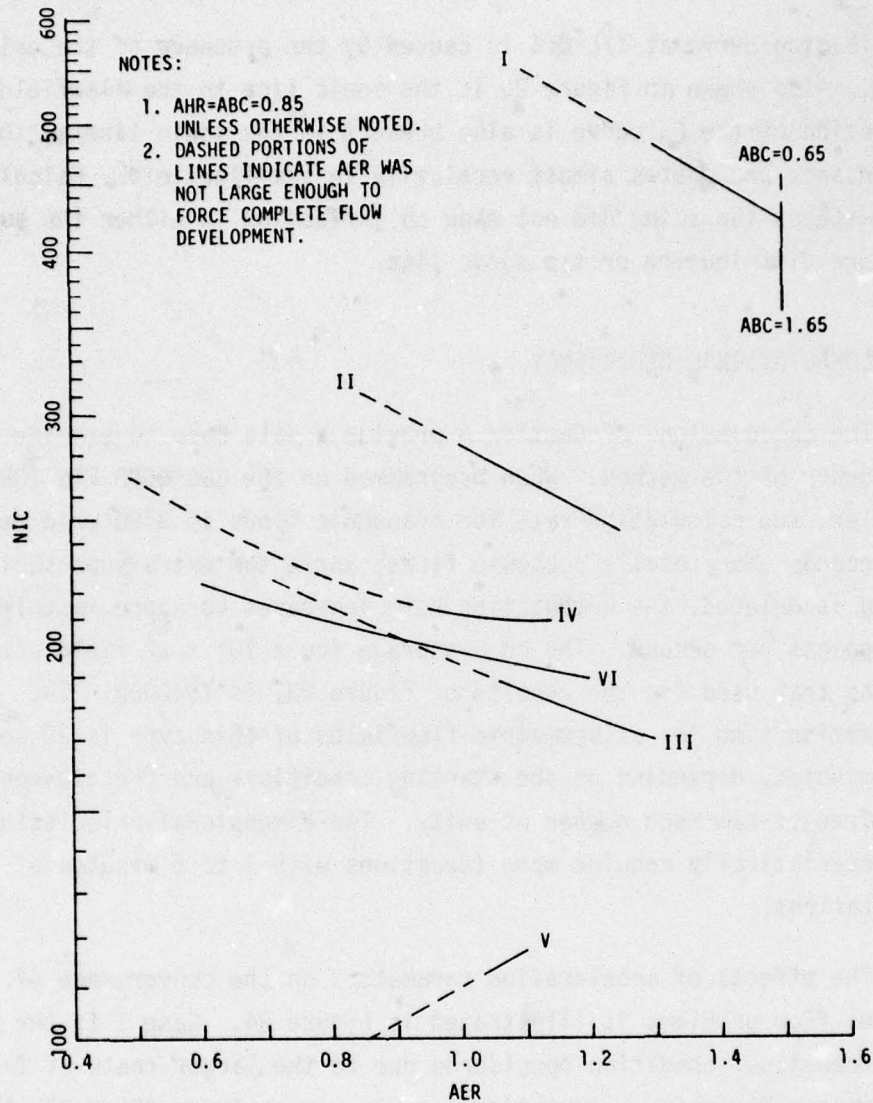Figure 23. Pressure Distribution and Sonic Line for M=0.975 Flow over a 10% Thick Parabolic Arc Body of Revolution

distribution curve at X/L=0.6 is caused by the presence of the cylindrical sting. Also shown in Figure 23 is the sonic line in the flowfield. The inflection of the C_p curve is also present in the sonic line as the disturbance propogates almost vertically in the flowfield. Calculations made without the sting did not show an inflection in either the surface pressure distribution or the sonic line.

2. COMPUTATIONAL EFFICIENCY

The calculations of Section A provide a data base to examine the efficiency of the method. When programmed on the CDC 6600 FTN (OPT=1) compiler, the calculation rate for transonic flows is 3700 grid points per second. For totally subsonic flows, where the extra supersonic coding is deleted, the computation rate increases to approximately 5000 grid points per second. The core storage for a 101 x 22 field size, such as that used for the results of Figure 23, is 154000B. The computation time for axisymmetric flowfields of this type is 30 seconds to 3 minutes, depending on the starting conditions and the closeness to a free-stream Mach number of unity. Two-dimensional calculations characteristically require more iterations with 1 to 5 minutes of computations.

The effects of acceleration parameters on the convergence of various flow problems is illustrated in Figure 24. Case I is the only two-dimensional condition considered due to the larger costs of 2-D solutions. The primary investigation was made holding ABC=0.85 while AER was varied from a low of 1.1 to a high of 1.5. When AER was raised above 1.5 the solution diverged, no matter what the value assigned to ABC. To study the effect of ABC at optimum AER, ABC was varied from 0.65 to 1.8. With ABC above 1.65, the calculations diverged. As can be seen from Figure 24, with the optimum acceleration parameters of AER=1.5 and ABC=1.65, NIC could be reduced to 355 with 103.1 seconds of CDC 6600 computation time. The worst case shown, AER=1.1, ABC=0.85, required 544 iterations and 157.6 seconds for an increase in time of 53%. The selection of optimum acceleration parameters is well worth the effort.

NOTES:
1. AHR=ABC=0.85
   UNLESS OTHERWISE NOTED.
2. DASHED PORTIONS OF
   LINES INDICATE AER WAS
   NOT LARGE ENOUGH TO
   FORCE COMPLETE FLOW
   DEVELOPMENT.

CASE	COORDINATE SYSTEM*	START CONDITION	END CONDITION	SOLUTION PLOT*
I	11	M=0.001	M=0.63	20
II	17	UNIFORM STREAM	M=0.8	21
III	SIMILAR TO 17		M=0.8	BODY OF 23
IV		↓	M=0.9	↓
V		M=0.8	M=0.9	
VI	↓	M=0.4	M=0.9	26

*Figure No.

Figure 24. Acceleration Parameter Study

Case II is an almost completely subsonic axisymmetric cone-cylinder-boattail configuration. AER was varied from 0.85 to 1.8 and ABC was varied from 0.6 to 1.1. Changing AER causes the expected trend in NIC; however, varying ABC did not affect the solution at all until it suddenly diverged when ABC was increased to 1.0 from 0.95.

Cases III, IV, and V are different conditions solved on the same body. In all three cases, ABC had no effect on the convergence until divergence occurred at a value of ABC near unity. Another problem which must be considered is that at the lower values of AER the solution will not develop as much as it will when accelerated near the limit. The dashed portions of the lines represent these areas. The less disturbed the field is (i.e., over a smooth axisymmetric body), the greater the problem. In Case I, the maximum discrepency in C_p on the body surface was only $\Delta C_p = 0.001$; but for Cases II, III, and IV, the value reached 0.009. To ensure the most correctly developed solutions, it is necessary to use a value of AER within 0.2 of the maximum allowable.

Case V presents an especially troublesome case, in which NIC increases as AER is increased. This phenomenon can be credited to the lower AER values damping out the small change in the flowfield when an M=0.9 solution is started from an M=0.8 solution. The calculation savings in obtaining the M=0.9 solution by the procedure of Case V is well worth the extra care that must be exercised in the selection of acceleration parameters. Prior knowledge of the effects of acceleration parameters on the acquisition of an acceptable solution is essential.

Case VI represents an $M_\infty = 0.9$ condition with a strong shock in the boattail region. The pressure distribution over the body is illustrated in Figure 26 . The maximum Mach number before the shock is 1.295. By using an optimum AER of 1.2 and ABC=AHR=0.85 the solution converged smoothly in 187 iterations. Although the error reached the convergence criteria when AER was set to 1.25, the maximum error was fluctuating as it did so on the 202nd iteration. Changing AHR and ABC had very little effect on the convergence until they caused divergence when set

to 1.0. The only effect shown was that convergence did require 197 iterations when AHR was reduced to 0.60 with AER=1.2 and ABC=0.85. A good characteristic that this solution did show, and which the other five cases lacked, was a satisfactory flow development with less than optimum values of AER.

3. BOATTAIL PRESSURE DRAG CALCULATIONS

A study of boattail pressure drag calculated by the inviscid flow analysis of this report was made using the experimental data of Reubush (Reference 17). The present method used to calculate pressure drag is discussed in Section III D.

Reubush ran several cone-cylinder, circular-arc boattail bodies with solid sting plume simulators in the NASA LaRC 16T wind tunnel. The maximum diameter of his body was 0.5 feet. The cone-cylinder fore-body arrangement was 4.0 feet to the start of the boattail. The flow region was simulated with a coordinate system similar to Figure 17. The upper boundary was set at the proper height to simulate the radius of the octagonal 16T test section. A solid-wall boundary condition was used to simulate the wall even though 16T has slotted walls. Two configurations were studied.

The first (illustrated in Figure 25) had a boattail length to maximum body diameter ratio (L/D) of 1.768. This boattail had a small separated flow region near the junction with the sting which starts at about station 1.6, as shown in Figure 25. Comparisons were made at flow Mach numbers of 0.4, 0.6, 0.8, 0.9, and 0.94. The present calculations are typical of inviscid boattail solutions (Figure 25). In the region ahead of the separation point, the pressure distributions compare very well. We would expect the drag integrations to this point to compare favorably. However, after this point, the inviscid solution continues to recompress while the actual flow separates and fails to recompress. The result is a lower drag prediction from the inviscid analysis. This fact is demonstrated by the drag plots of Figure 27. All across the Mach number range, the inviscid drag is lower than the experimental drag.
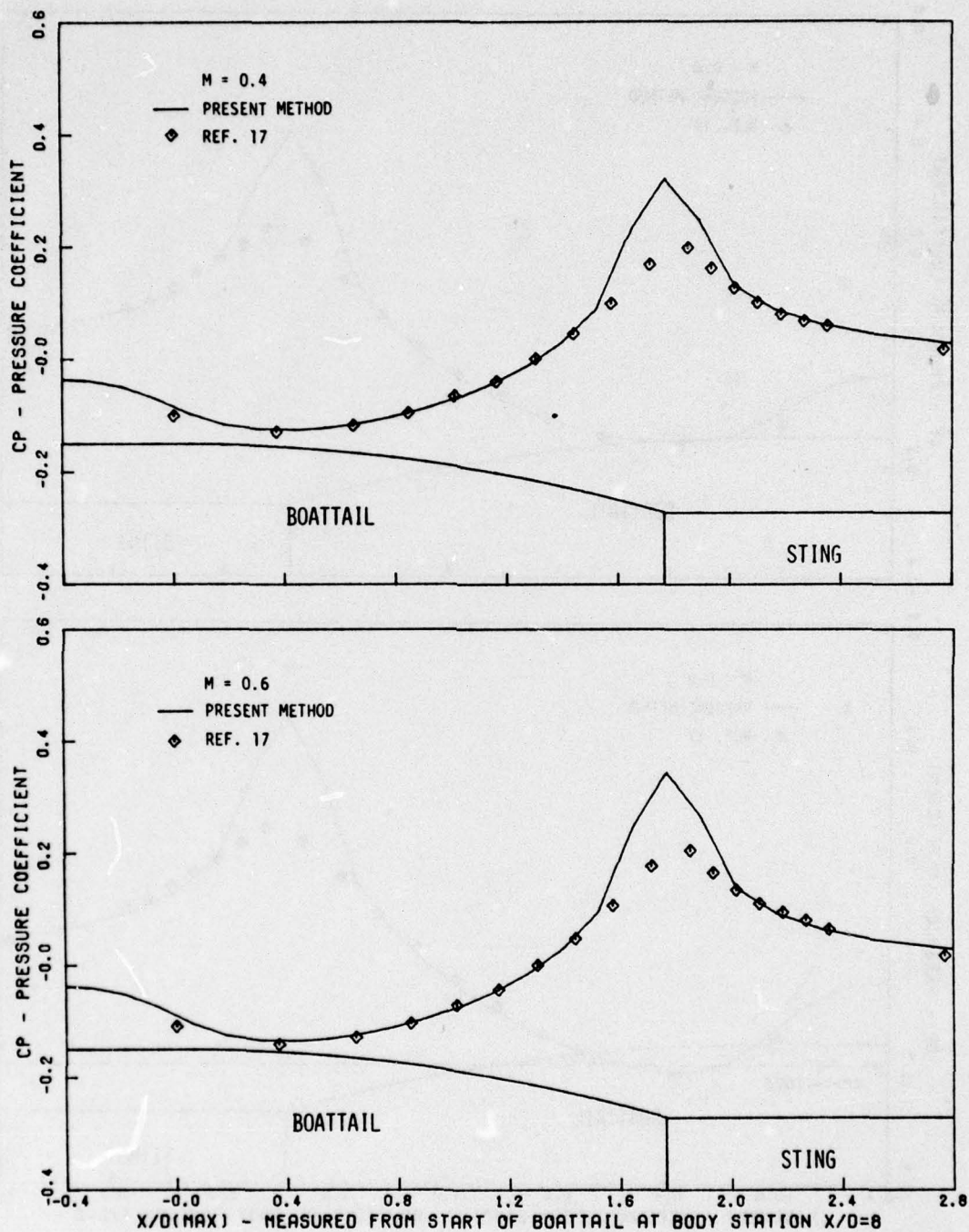
Figure 25. Pressure Distributions for Flow over the NASA Langley Circular Arc Boattail (L/D = 0.8) at M=0.4, 0.6, 0.8, 0.9, and 0.94
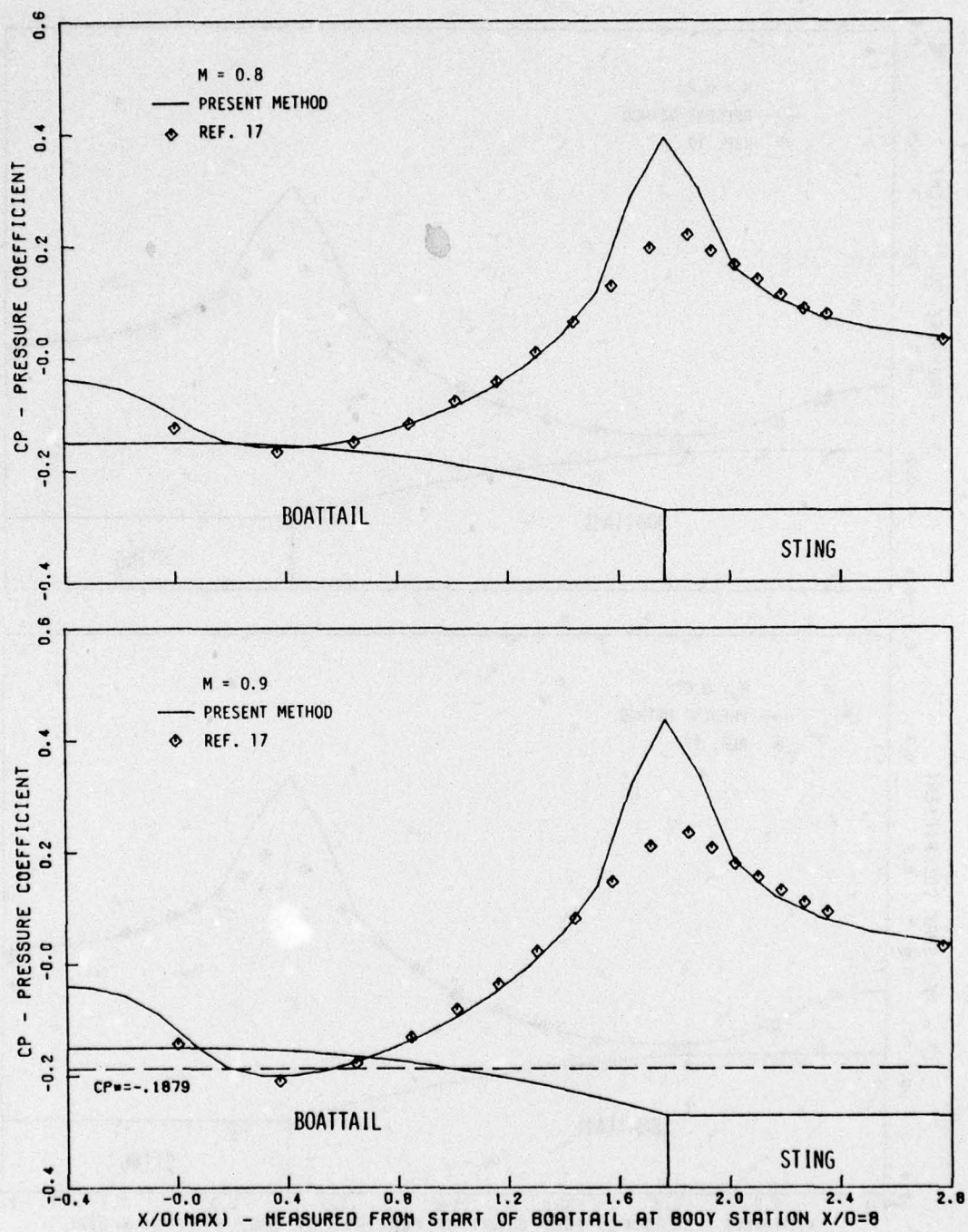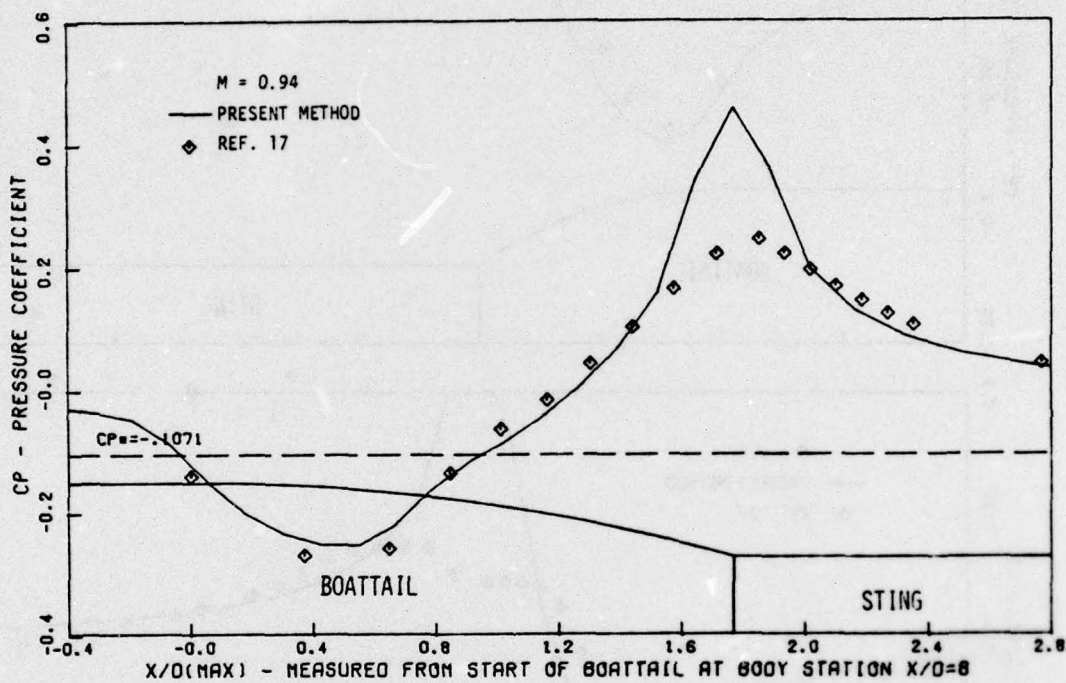
Figure 25. (Continued)
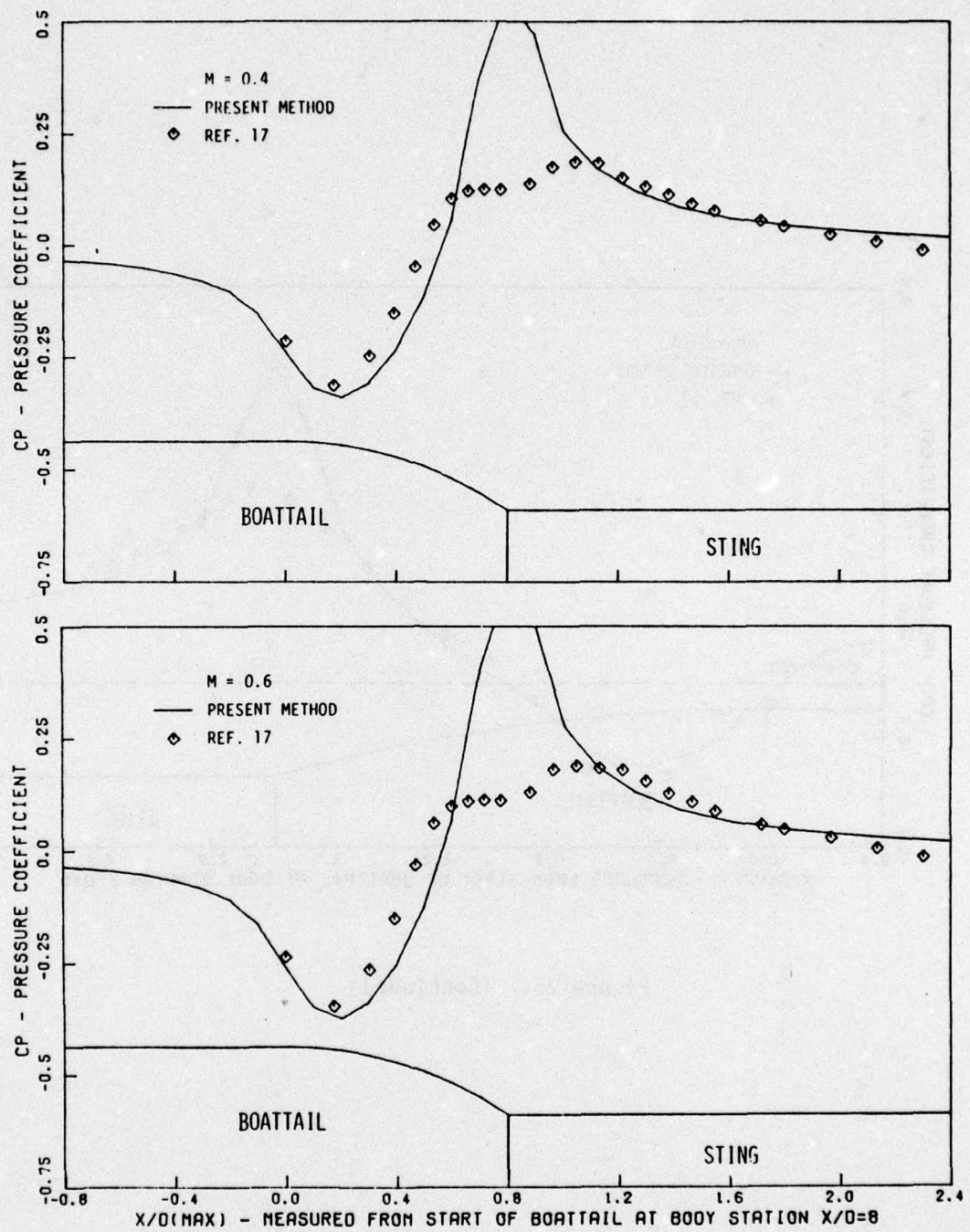
Figure 25. (Concluded)

Figure 26. Pressure Distributions for Flow over the NASA Langley
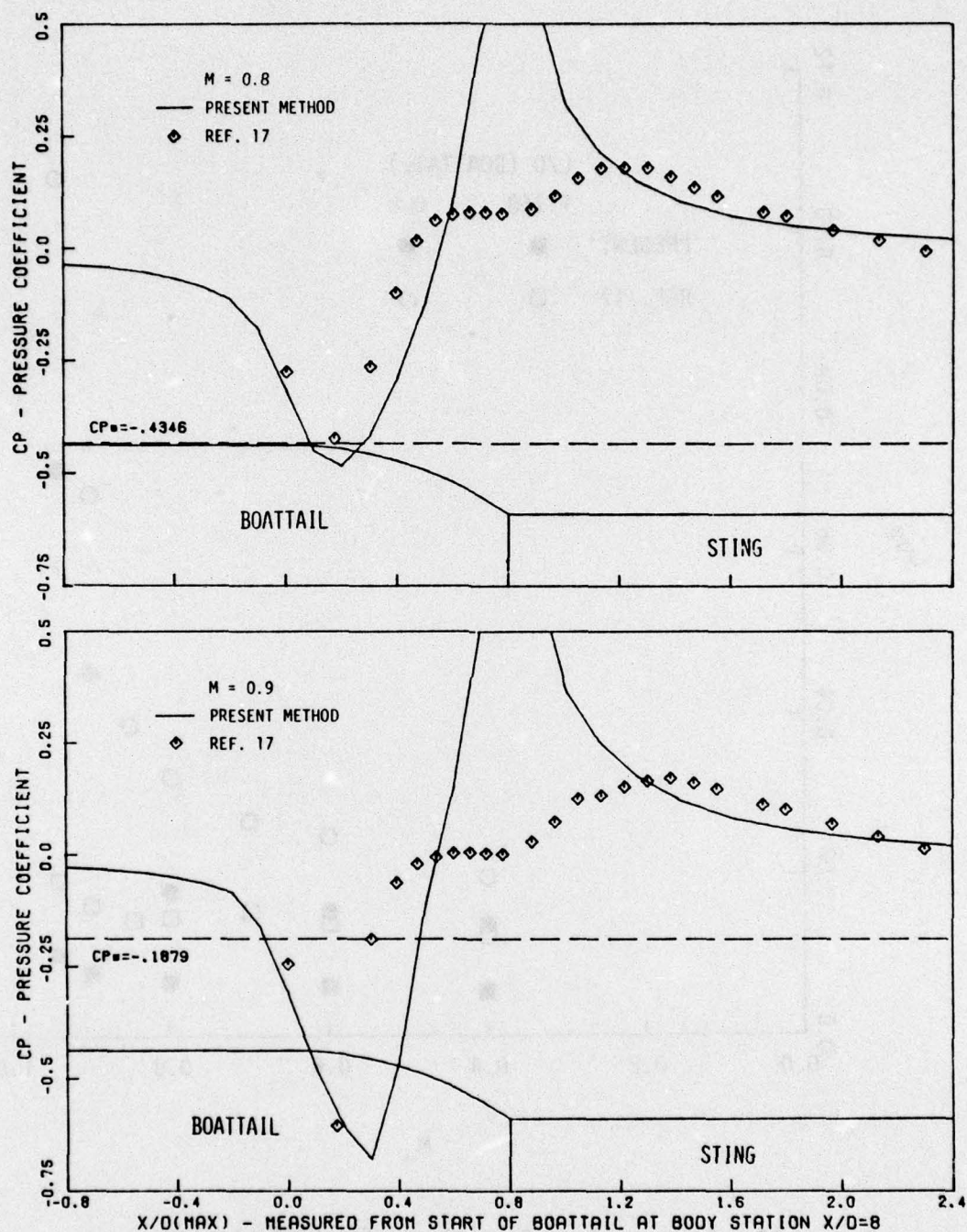Circular Arc Boattail (L/D = 0.8) at M=0.4, 0.6, 0.8,
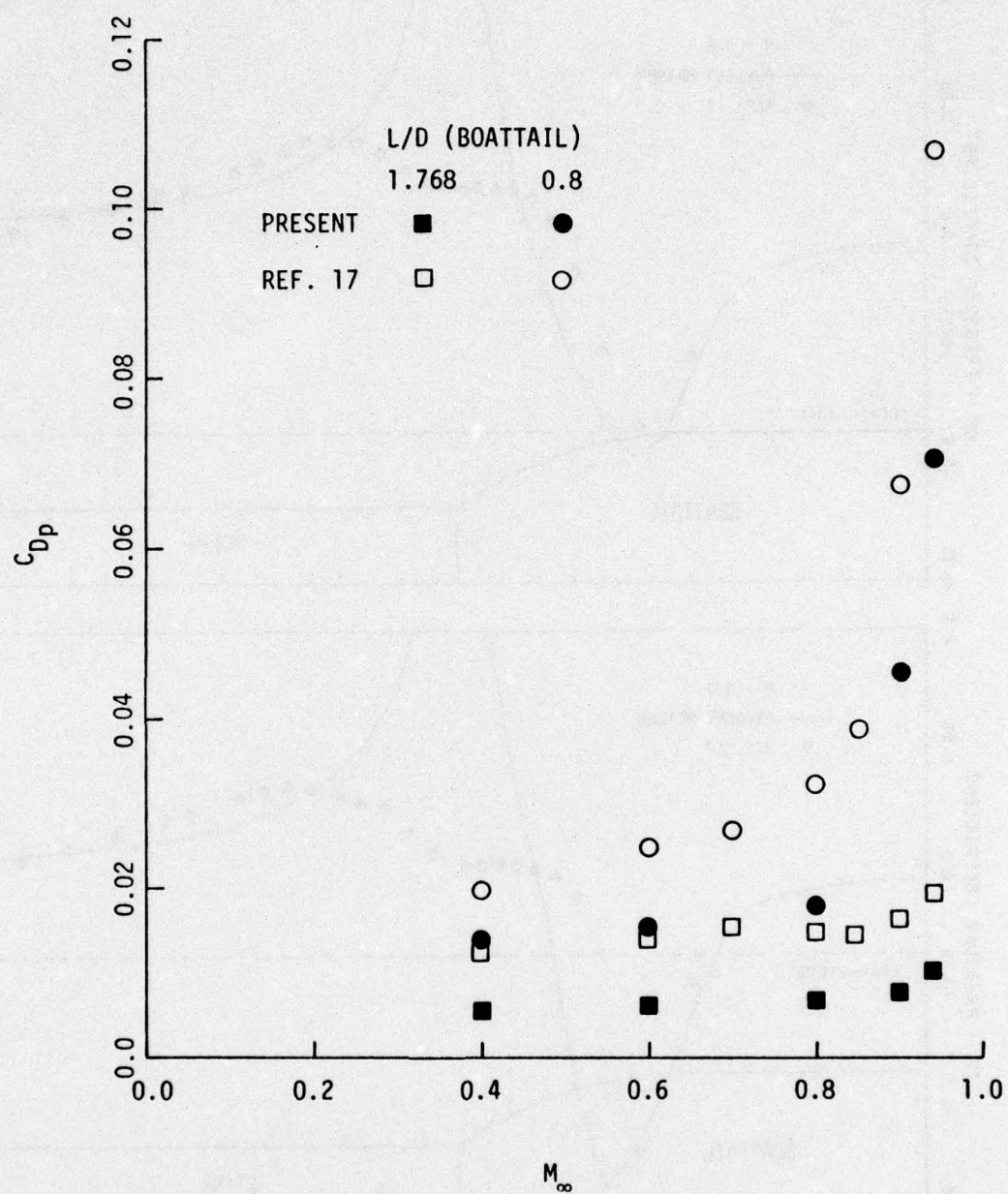and 0.9

60

Figure 26. (Concluded)

Figure 27.   Pressure Drag Comparisons for NASA Langley
            Circular Arc Boattails

The second configuration featured a much shorter boattail with L/D=0.8. It was expected that the inviscid analysis would not predict the pressure distribution over this highly viscous influenced boattail flowfield very well. Comparisons were made at Mach numbers of 0.4, 0.6, 0.8, and 0.9. The present results and Reubush's experimental data are plotted in Figure 26. For M=0.4, the pressure distributions compare well up to the separation point. From there on, the experimental data levels out over the separation region and the inviscid analysis rises to a typical large recompression value. As expected, the drag predictions by the invicid analysis are lower than the values calculated from the experimental pressure distributions. The same trend continues through M=0.8. The calculations overshoot the experimental pressures upstream of the separation point and cause a calculated drag increase; the calculated recompression error grows and causes an even larger calculated drag reduction. At M=0.9, a shock has formed on the boattail, and due to the large viscous effects the calculation does not compare well aft of X/D(MAX)>0.3. However, note that drag rise is predicted by the invicid analysis as drag increases drastically near M=0.9.

Although the invicid drag values do not predict the exact magnitude of the experimental drag, the method does predict the drag trends and drag rise with reasonable accuracy.

4. UPPER BOUNDARY CONDITION EFFECTS

Experimental studies have been made with various testing techniques to examine the performance of aircraft nozzle afterbodies (NAB). These testing techniques involved the application of various upper boundary conditions to the fluid flow problem as well as different support and jet plume simulation methods. The present method is used to examine the trends exhibited by two of these testing techniques.

First, a description of the two test configurations is in order. Bittrick (Reference 18) made a study of NAB drag using a free jet model technique. The General Dynamics Free Jet Duct Calibration Facility was used with the NAB attached to a strut-supported hollow shaft that

located the model centrally in the 9.25 inch square test section. Jet
flow to the nozzle was supplied through the shaft. The boundary layer
entering the NAB region on the model developed along a 4.0 foot growth
run at $R_e \approx 5.5 \times 10^6$. The maximum diameter of the model was 3.55 inches.
The model extended 9.05 inches past the end of the square test section.

Bowers (Reference 19) tested a similar NAB contour, using an annular
blowing sting technique. The 28.68 inch cone-cylinder-boattail model
was sting-mounted in the Air Force Flight Dynamics Laboratory Trisonic
Gasdynamics Facility. The facility is a closed circuit, variable pres-
sure wind tunnel with a solid wall 2.0 foot square test section. The
jet flow was supplied through the hollow sting and blown back annularly
around the sting to simulate the nozzle exhaust. At the M=0.8 test
condition considered, $R_e \approx 2.0 \times 10^6$. The maximum diameter of the model
is 3.75 inches, and the length of the NAB is 5.02 inches. Bowers ob-
tained his NAB coordinates from a blueprint of Bittrick's model.

A study using the analysis described in Section III was made on
three upper boundary configurations at M=0.8. The coordinates for the
calculation were obtained from construction specification dimensions
from Bowers' NAB test. The nominal upper boundary condition for the
potential flow is a simulated free air boundary calculated by placing
a solid-wall boundary condition, Equation 49, at 2.0 body lengths
(57.36 inches) radius. Even with this free-air boundary, the flow over
the mid section of the body did not quite reach the free-stream value.
At body station 17.0 inches, the minimum Mach number on the body was
calculated to be 0.806. This theoretical result indicates that the
fineness ratio of the body (7.6) was not quite large enough to ensure
that the approach Mach number to the NAB was independent of forebody
shape. The NAB surface pressure distribution for the free-air upper
boundary case is plotted in Figure 28 and flowfield Mach number contours
are plotted in Figure 29.

The next upper boundary condition calculated was designed to simu-
late the AFFDL 2.0 foot wind tunnel configuration. Here, as with the
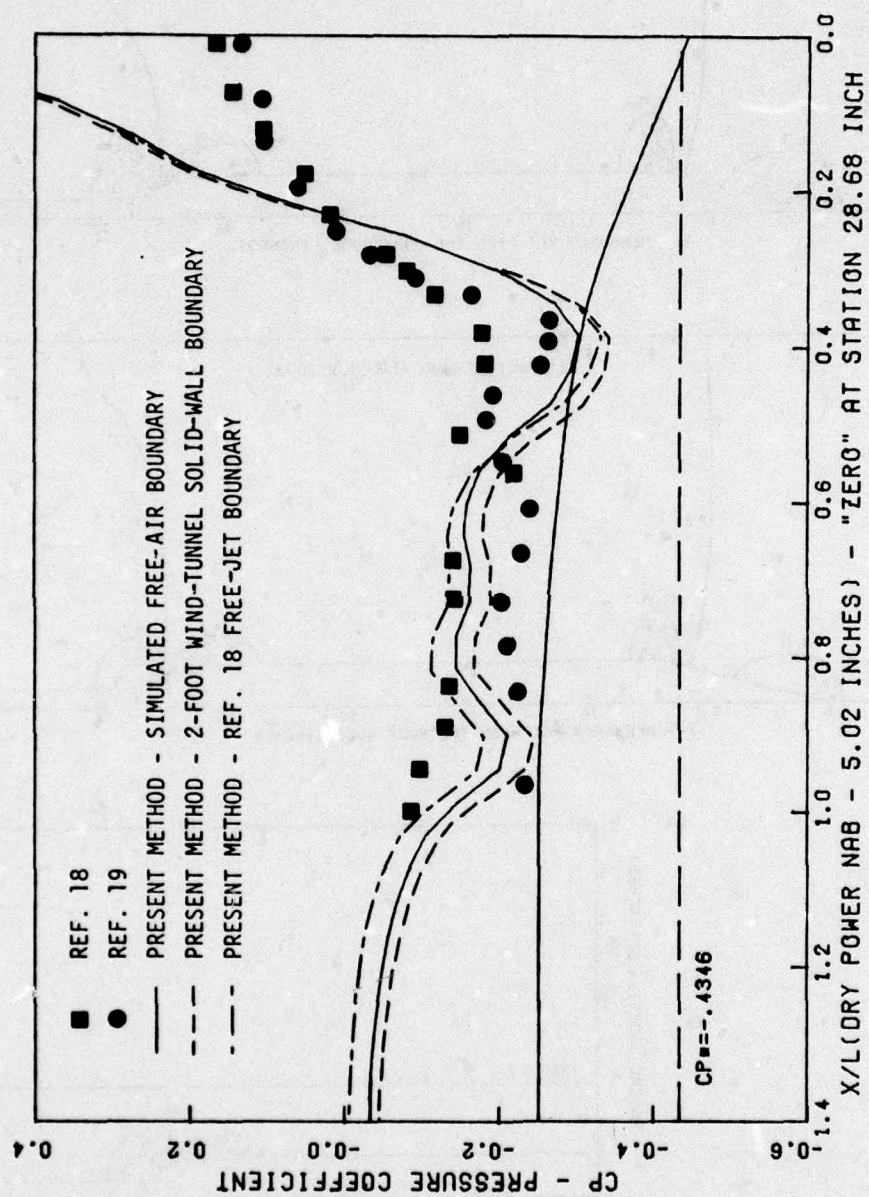nominal condition, the exhaust plume was simulated with a cylinder of

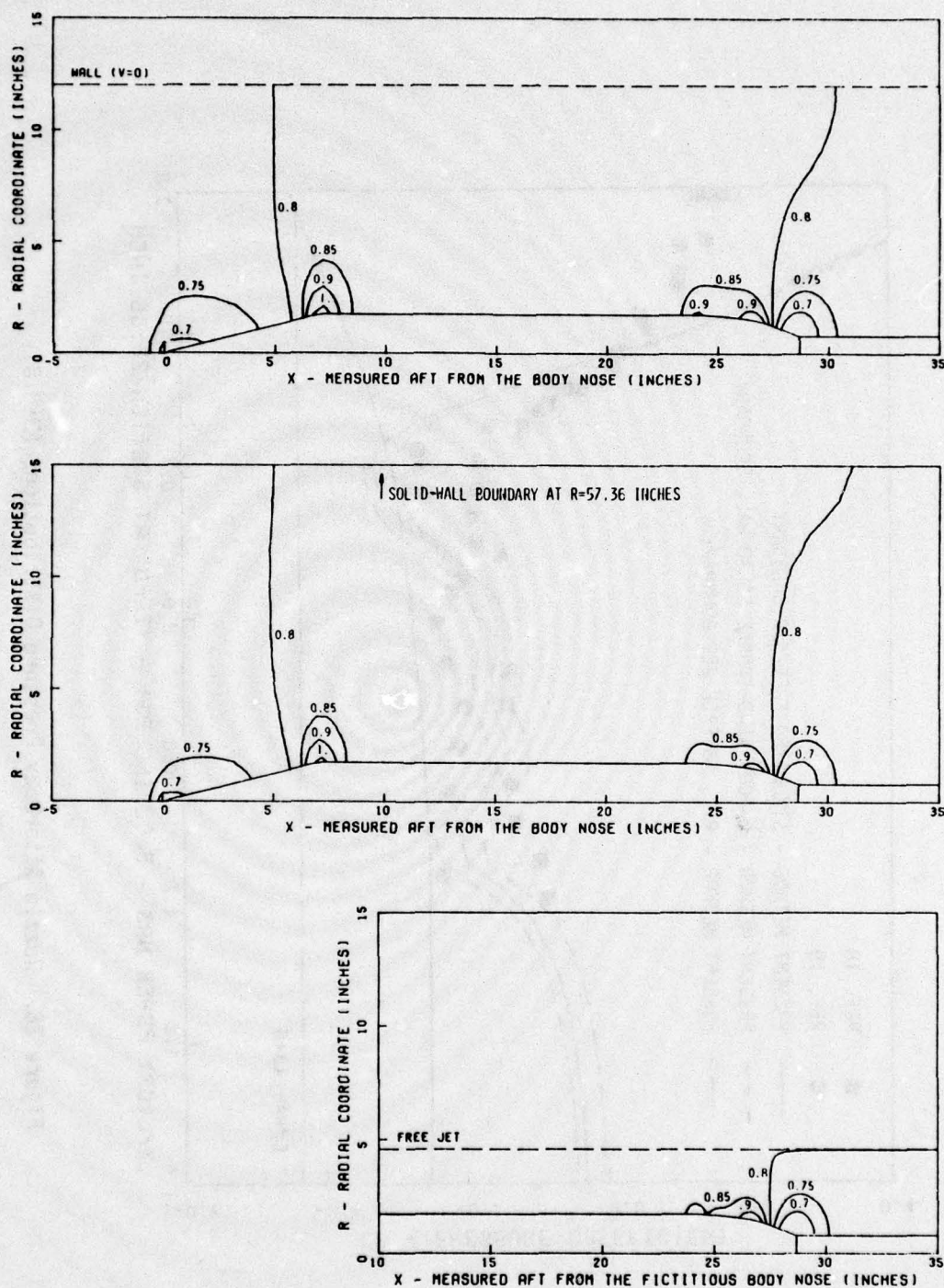Figure 28. Nozzle Afterbody Pressure Distributions (M=0.8)

Figure 29. Boundary Condition Effects on Nozzle Afterbody
Model Flow Field Mach Number Contours

the same diameter as the NAB jet exit. Both plots are again presented
in Figures 28 and 29. The calculated pressure distribution indicates
that the solid-wall upper boundary at 1.0 foot radius from the center-
line forces the flow to accelerate slightly over the body. The minimum
Mach number on the body was 0.814 which occurred at the 17.7 inch body
station. The approach Mach number to the NAB was correspondingly higher.

The final upper boundary condition calculated was modeled after the
free-jet setup of Bittrick. This calculation was made with no forebody.
The upstream boundary condition of a uniform stream at M=0.8 was applied
at an effective body station of 10.0 inches. The free-jet boundary was
approximated by placing a straight horizontal boundary at R/D(MAX)=1.305.
The free-jet boundary has been approximated by Murman (Reference 20) in
small perturbation theory by setting the perturbation velocity equal to
zero. For this method, the corresponding treatment was to solve $u=u_\infty$
along the free-jet boundary. The NAB coordinates were the same as those
used in the other calculations. The calculated Mach number at the 17.0
inch body station is 0.80001. Therefore, the approach Mach number to
the NAB is very close to the desired value of 0.8. The calculated pres-
sure distribution and Mach number contours are presented in Figures 28
and 29.

A comparison of the calculated flowfields may be made by consider-
ing the Mach number contour plots in Figure 29. Note that the place-
ment of the solid wall at the 12.0 inch position causes a growth of
the supersonic pocket at the shoulder and the appearance of a new M=0.9
contour in the NAB region as compared to the free-air case. The free-
jet case predicts a further reduction in the size of the contours.

In addition to the calculated surface pressure distributions
plotted in Figure 28, the experimental data of Bittrick and Bowers
are plotted for M=0.8 and NPR≈2.0. It is felt that comparisons of
the experimental and analytical pressure distributions are only valid
over the first part of the NAB as viscous smoothing effects and the
imprecise body coordinate definition are considerable factors in
transonic NAB flow. It can be seen that the calculated pressures
for the 2.0 foot configuration and Bowers' data compare well near X/L=1.0.

Also, the level of the calculated pressures for the free-jet case
compare well with Bittrick's data for X/L>0.6, except for the dip
in the calculated pressure at X/L=0.95. It is expected that this is
due to a combination of viscous smoothing and an actual difference
in NAB coordinates at the position.

The above analysis has shown that the present analytical method
is capable of correctly handling various upper boundary conditions
to aid in the interpretation of NAB model test data from various
techniques.

SECTION V

SUMMARY

The exact velocity potential equation for steady, two-dimensional and axisymmetric flow in simply connected regions has been solved with the use of automatically generated body-fitted curvilinear coordinates from incompressible conditions to Mach numbers near unity. The following is a summary of the results of this effort:

1. The definitions of the attraction factors, P and Q, as developed by Thompson (Reference 1) have been improved to ensure predictable results when generating coordinates that involve attraction to both upper and lower boundaries.

2. A new, fast system of generating near orthogonal coordinates for moderately thick (D/L < 0.3) bodies has been developed and proven to be reliable.

3. The potential solution developed has been shown to be accurate and reasonably efficient for a wide variety of body shapes, boundary conditions, and Mach numbers.

4. An axisymmetric body pressure drag integration method has been applied and has been shown capable of accurately predicting drag rise and drag trend.

5. The implementation of various boundary conditions has proved it possible to simulate various wind-tunnel testing techniques.

REFERENCES

1. J. F. Thompson, F. C. Thames, and C. W. Mastin, "Automatic Numerical Generation of Body-Fitted Curvilinear Coordinate System for Fields Containing Any Number of Arbitrary Two-Dimensional Bodies," Journal of Computational Physics, Vol 15, No. 3, July 1974.

2. F. C. Thames, "Numerical Solution of the Incompressible Navier-Stokes Equations about Arbitrary Two-Dimensional Bodies," PhD Dissertation, Mississippi State University, May 1975.

3. U. Ghia, J. K. Hodge, and W. L. Hankey, "An Optimization Study for Generating Surface-Oriented Coordinates for Arbitrary Bodies in High Re-Flow," To be published as an AFFDL TR, 1977.

4. J. F. Thompson, F. C. Thames, and C. W. Mastin, "Boundary Fitted Curvilinear Coordinate Systems for Solution of Partial Differential Equations on Fields Containing any Number of Arbitrary Two-Dimensional Bodies," NASA-CR-2729.

5. H. W. Liepmann, and A. Roshko, Elements of Gasdynamics, John Wiley & Sons, Inc., New York, 1957.

6. E. M. Murman, and J. D. Cole, "Calculation of Plane Steady Transonic Flows," AIAA J., Vol 9, No. 1, Jan 1971.

7. E. M. Murman, and J. A. Krupp, "Solution of the Transonic Potential Equation using a Mixed Finite Difference System," Proceedings of the 2nd International Conference on Numerical Methods in Fluid Dynamics, Lecture Notes in Physics, Springer-Verlag, 1971.

8. K. Karamcheti, Principles of Ideal-Fluid Aerodynamics, John Wiley & Sons, Inc., New York, 1966

9. I. H. Abbott, and A.E. Von Doenhoff, Theory of Wing Section, Dover Publications, Inc., New York, 1959.

10. W. H. Lowe, "Two-Dimensional Wind Tunnel Tests of a NACA 0012 Airfoil at High Reynolds Number," General Dynamics Report HST-TR-360-5, Sep 1973

11. R. J. Vidal, P. A. Catlin, and D. W. Chudyk, "Two-Dimensional Subsonic Experiments with a NACA 0012 Airfoil," Calspan Report No. RK-5070-A-3, Dec 1973.

12. NASA Langley, "Improved Nozzle Testing Techniques in Transonic Flow," Unpublished data, Nov 1973.

13. J. L. Hess, and A. M. O. Smith, "Calculation of Potential Flow About Arbitrary Bodies," Progress in Aeronautical Sciences, Vol 8, Pergamon Press, Inc., c. 1967, pp 1-138.

REFERENCES (CONTINUED)

14. Arnold Engineering Development Center, AGARD NAB Study (Phase I) In the Propulsion Wind Tunnel (16T), Test Plan - TF337, Feb 1974.

15. Robert A. Taylor, and John B. McDevitt, "Pressure Distributions at Transonic Speeds for Parabolic - Arc Bodies of Revolution Having Fineness Ratios of 10, 12, and 14," NACA TN 4234, 1958.

16. Frank R. Bailey, "Numerical Calculation of Transonic Flow About Slender Bodies of Revolution," NASA TN D-6582, 1971.

17. David E. Reubush, "Experimental Study of the Effectiveness of Cylinderical Plume Simulators for Predicting Jet-On Boattail Drag at Mach Numbers Up to 1.30," NASA TN D-7795, 1974

18. W. C. Bittrick, "Lightweight Fighter Nozzle Model Test with Faired Aft-Fuselage," General Dynamics Corporation, MR-P-348, Feb 1973.

19. Douglas L. Bowers, "Investigation of the Annular Sting Support Concept for Aftbody Nozzle Testing," AIAA Paper No. 77-961, AIAA/SAE 13th Propulsion Conference, Orlando, Florida, July 1977.

20. Earll M. Murman, Frank R. Bailey, and Margaret L. Johnson, "TSFOIL- A Computer Code for Two-Dimensional Transonic Calculations, Including Wind-Tunnel Wall Effects and Wave-Drag Evaluation," NASA SP 347, March 1975.

21. Antony, Jameson, "Iterative Solution of Transonic Flows Over Airfoils and Wings, Including Flows at Mach 1," Communications on Pure and Applied Mathematics, Vol XXVII, 1974.

22. F. C. Thames, J. F. Thompson, C. W. Mastin, and R. L. Walker, Accepted for publication in "J. of Comp. Phys.," 1977.

23. J. K. Hodge, "Numerical Solution of Incompressible Laminar Flow About Arbitrary Bodies in Body-Fitted Curvilinear Coordinates," PhD Dissertation, Mississippi State University, 1975.